NANO · MICRO small
www.small-journal.com

Commensurate, Incommensurate, and Reconstructed Structures of Multilayer Transition Metal Dichalcogenide and Their Applications

Hyun-Geun Oh, Younghyun You, Seungyun Lee, Sangheon Lee, Fan Ren, Stephen J. Pearton, Jihyun Kim,* and Gwan-Hyoung Lee**

Multilayer transition metal dichalcogenides (ML-TMDs) with commensurate, incommensurate, and reconstructed structures, have emerged as a class of 2D materials with unique properties that differ significantly from their monolayer counterparts. While previous research has focused on monolayers, the discovery of various novel properties has sparked interest in multilayers with diverse structures engineered through stacking. These materials are characterized by interactions between layers and exhibit remarkable tunability in their structural, optical, and electronic behaviors depending on stacking order, twist angle, and interlayer coupling. This review provides an overview of ML-TMDs and explores their properties such as electronic band structure, optical responses, ferroelectricity, and anomalous Hall effect. Various synthetic methods employed to fabricate ML-TMDs, including mechanical stacking and chemical vapor deposition techniques, with an emphasis on achieving precise control of the twist angles and layer configurations, are discussed. This study further explores potential applications of ML-TMDs in nanoelectronics, optoelectronics, and quantum devices, where their unique properties can be harnessed for next-generation technologies. The critical role played by these materials in the development of future electronic and quantum devices is highlighted.

1. Introduction

Transition metal dichalcogenides (TMDs) have garnered significant attention over the past decade due to their versatile properties, including their semiconducting, metallic, and superconducting properties.[1–9] These layered materials, represented by the general formula MX_2 (where M is a transition metal and X is a chalcogen), feature strong in-plane covalent bonds and weak out-of-plane van der Waals (vdW) interactions, making them highly suitable for mechanical exfoliation and the creation of atomically thin layers. Research on TMDs initially began with monolayer systems, which exhibited remarkable properties, such as vdW surface, direct bandgaps, and strong excitonic effects.[10–23] These discoveries have since paved the way for extensive studies on multilayer TMDs, unveiling new physical phenomena arising from interlayer interactions.[6,24–27] In multilayer

H.-G. Oh, G.-H. Lee
Department of Materials Science and Engineering
Seoul National University
Seoul 08826, Republic of Korea
E-mail: gwanlee@snu.ac.kr

Y. You, S. Lee, J. Kim
HBM Package Development Group
Samsung Electronics
Suwon 16677, Republic of Korea
E-mail: jihyunkim@snu.ac.kr

The ORCID identification number(s) for the author(s) of this article can be found under https://doi.org/10.1002/smll.202412737

DOI: 10.1002/smll.202412737

Y. You, S. Lee, J. Kim
Department of Chemical and Biological Engineering
Seoul National University
Seoul 08826, Republic of Korea

S. Lee
Department of Chemical Engineering and Materials Science
Ewha Womans University
Seoul 03760, Republic of Korea

F. Ren
Department of Chemical Engineering
University of Florida
Gainesville, FL 32611, USA

S. J. Pearton
Department of Materials Science and Engineering
University of Florida
Gainesville, FL 32611, USA
E-mail: spear@mse.ufl.edu

(ML)-TMDs, the relative alignment between adjacent layers plays a crucial role in determining their electronic, optical, and mechanical properties. Specifically, the stacking configuration can be either commensurate, where the layers are aligned in a well-ordered, periodic structure, or incommensurate, where a misalignment such as a twist angle or lattice mismatch leads to a moiré pattern. These commensurate and incommensurate ML-TMDs exhibit vastly different behaviors owing to the subtle interplay between interlayer interactions, strain, and symmetry-breaking effects.

In this review, we present a detailed examination of the current understanding of ML-TMDs, focusing on their structural, optical, and electronic properties. We also explore the synthetic techniques developed to produce these materials with controlled properties and their potential applications in technologies including field-effect transistors (FETs), optoelectronic devices, and quantum information processing systems. By combining the latest research in this rapidly evolving field, this review seeks to provide a comprehensive foundation for the further exploration and technological exploitation of ML-TMDs.

2. Structural Classification of ML-TMDs

ML-TMDs can be classified into "commensurate" and "incommensurate" states depending on their stacking registry and the relative alignment between adjacent layers. The "commensurate state" is defined as the structure that has perfectly aligned arrangements corresponding to the lowest energy configuration including two main types of stacking arrangements: rhombohedral (3R) and hexagonal (2H) structures. The "incommensurate state," in contrast, is defined as the structure that has a higher energy state compared to the commensurate state and exhibits a moiré pattern, which is a periodic interference pattern that emerges due to the mismatch in lattice orientation with the twist angle or lattice parameters in vertically stacked hetero-multilayer TMDs.

The 3R structure shown in **Figure** 1a is characterized by each monolayer being aligned in a single direction with a 0° twist angle and an in-plane-shifted arrangement (C_{3v}). In this configuration, the layers are stacked such that the top layer atoms are displaced relative to the bottom layers, leading to a low-energy arrangement. In contrast, the 2H structure shown in Figure 1b has a 60° twist angle between the layers and a hexagonal configuration (D_{6h}), where the metal atoms in each layer are positioned directly above or below the chalcogen atoms of the adjacent layers. This arrangement leads to highly symmetric and energetically favorable stacking in the 2H structure. In contrast, if ML-TMDs possess a stacking angle other than 0° or 60° or if they form heterostructures with lattice parameter mismatches between the layers, they form an incommensurate state with a moiré superlattice, as shown in Figure 1c. The incommensurate state is energetically higher than the commensurate state and is characterized by more complex local structural distortions due to the twist and strain within the layers, as shown in the calculated total van der Walle (vdW) energy as a function of the twist angle (θ) in Figure 1d.[28–31]

It has been reported that there exist critical angles (θ_c^R and θ_c^H near 0° and 60°, respectively) at which the system exhibits its highest energy state and maximal average local strain near 0° and 60° twist angles (Figure 1d).[29–33] Below these angles, the structure is unstable, leading to spontaneous reconstruction to reduce the total energy and alleviate the lattice strain. The "reconstructed state" is defined as the structure consisting of commensurate domains and incommensurate domain walls that results from the reconstruction of ML-TMDs with twist angles below the critical angles. For angles $0° < \theta < \theta_c^R$ (R-type), the ML-TMDs are reconstructed into arranged commensurate MX and XM domains, which have the lowest energy with alternating triangular configurations separated by incommensurate domain walls known as saddle points (SPs), as shown in the reconstructed R-type polydomain structure of Figure 1e. The presence of these saddle points allows for some flexibility in the system, which helps to relieve the strain in commensurate regions.[31,33,34] Meanwhile, for angles close to $\theta_c^H < \theta < 60°$ (H-type), the reconstructed H-type polydomain structure forms commensurate hexagonal XMMX domains, separated by incommensurate SPs as depicted in Figure 1f. These domains are arranged in a honeycomb-like pattern, providing another pathway for strain relief.[31,33,34] As theoretical studies have shown, the balance between the commensurate domains and the incommensurate domain walls is critical for determining the structural and electronic properties of the system.[29–32,35–38] **Table** 1 summarizes the twist angles of reconstructed ML-TMDs used in previous experimental studies. As the twist angle approaches 30° at $\theta_c^R < \theta < \theta_c^H$, the size of the commensurate domains steadily decreases, while the width of the incommensurate domain walls grows. Eventually, at sufficiently high twist angles, the system reaches a fully incommensurate moiré superlattice. In this state, the layers exhibit large interlayer spacing and a rigid, nearly flat lattice structure owing to the loss of registry between the layers.[30,39]

Interestingly, intermediate-energy valleys were observed for twist angles above the critical angle (Figure 1d). These energy valleys correspond to metastable configurations, in which the system relaxes into a state with moderate energy. The initial unrelaxed twisted ML-TMDs near these angles tend to relax toward these intermediate energy states rather than reverting to commensurate 0° or 60° configurations. This behavior introduces a degree of twist angle insensitivity, indicating that the electronic and structural properties of ML-TMDs can remain within a broad range of twist angles.[40–42] This characteristic enables ML-TMDs to display unique electronic phenomena such as the formation of flat electronic bands, which are associated with exotic states such as superconductivity, Mott insulating behavior, and the anomalous Hall effect (AHE).

In summary, ML-TMDs can be categorized into commensurate and incommensurate states based on their stacking configuration. The commensurate state includes low energy 3R and 2H stacking, while the incommensurate state features moiré patterns that emerge due to either a twist angle or a lattice mismatch. At the critical angles (θ_c^R, θ_c^H), the system reaches its highest energy state. When the twist angle decreases below the critical angle for R-type ($0° < \theta < \theta_c^R$) or increases above the critical angle for H-type ($\theta_c^H < \theta < 60°$), spontaneous reconstruction occurs, forming commensurate domains separated by incommensurate domain walls.[28–31] The electronic properties evolve with structural changes induced by the twist angle, leading to the emergence of unique characteristics. The following section will explore these characteristics in detail.

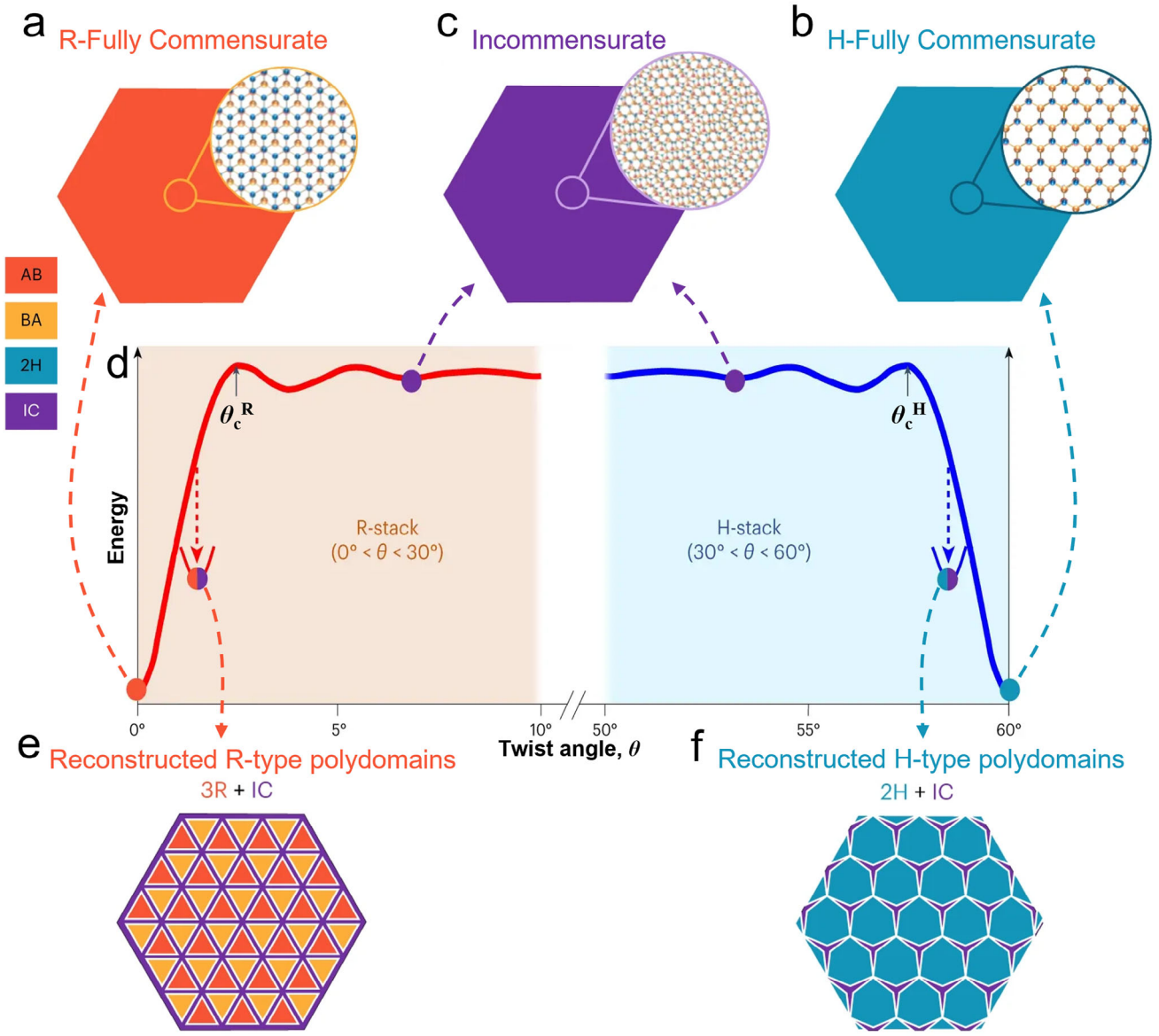

Figure 1. Schematics of the atomic structures of twisted TMDs with different stacking types and twist angles: a) R-fully commensurate, b) H-fully commensurate, c) incommensurate (IC), e) reconstructed R-type polydomains with 3R + IC, f) reconstructed H-type polydomains with 2H + IC. d) Schematics of the total vdW energy of twisted ML-TMDs as a function of the twist angle and angle-dependent atomic reconstruction. a–f) are reproduced with permission.[31] Copyright 2023, Springer Nature.

3. Properties of Commensurate, Incommensurate, and Reconstructed ML-TMDs

3.1. Band Structures

One of the unique differences between monolayers and ML-TMDs is the transition from direct to indirect bandgap as the number of layers increases. In monolayer TMDs, the conduction band minimum (CBM) and valence band maximum (VBM) are located at the $\pm K$ points in the Brillouin zone, resulting in a direct bandgap. This direct-bandgap configuration results in strong photoluminescence (PL), rendering monolayer TMDs highly suitable for optoelectronic applications.[43] As more layers are added, the electronic band structure undergoes significant changes owing to strong interlayer coupling. In ML-TMDs, the valence band maximum (VBM) moves from *K*-point to the Γ-point, transforming the bandgap into an indirect one.[44–49] This shift occurs because the interlayer coupling affects the states at the Γ-point. At the Γ-point, the atomic orbitals that form the valence band (mainly the chalcogen p-orbitals) experience stronger interlayer coupling because these orbitals overlap more effectively in the out-of-plane direction. This enhances overlap at the Γ-point lowers the energy of the states at that location, making the Γ-point states more energetically favorable than those at the

Table 1. Summary of critical twist angles at that atomic reconstruction occurs for ML-TMDs.

References	Materials	Stacking order	Twist angle θ
[33]	MoS_2/MoS_2	R	<2°
	WS_2/WS_2	H	>59.1°
	WS_2/MoS_2		
[34]	$WSe_2/MoSe_2$	R	≤1°
		H	≥59°
[40]	WSe_2/WSe_2	H	>57°
[124]	MoS_2/MoS_2	R	<0.1°
[125]	$MoSe_2/MoSe_2$	R	<0.25°
	WSe_2/WSe_2		
[126]	WSe_2 trilayer	R	<0.23°

K-point. As a result, the VBM shifts from the *K*-point to the Γ-point. For example, in the case of MoS_2, the bandgap decreases from ≈1.8 eV in the monolayer to ≈1.2 eV in the bulk form, transitioning from a direct to an indirect bandgap.[48] Similarly, it should be noted that interlayer coupling is responsible for the thickness- and twist angle-dependent behaviors. In ML-TMDs, charge carriers (electrons and holes) are no longer confined to a single layer and spread across multiple layers, leading to delocalized electronic states. This delocalization results in changes in the band structure and creates opportunities for manipulating the electronic properties through external factors such as electric fields.[50–52]

In this section, we explore the influence of different stacking types and spin–orbit coupling (SOC) on the electronic band structures of ML-TMDs. In each layer of ML-TMDs, the *d*-orbitals of the transition metals play a significant role in the conduction and valance bands (CB and VB, respectively) at the ±*K* points. Therefore, variations in the environment around the transition metal (M) atoms can lead to the splitting of the band structure.[53] In the 3R-stacking type, M atoms experience different environments in the top and bottom layers (one layer with and the other without facing adjacent M and X atoms), causing crystal field splitting and altering the band structure (**Figure 2a**). The band-edge energies in both the conduction band (CB) and valence band (VB) are localized in the top and bottom layers, respectively. When SOC occurs, spin–orbit splitting and spin-polarization take place in all bands except those in the Γ-*M* direction due to the lack of inversion symmetry. In the CB, the SOC strength is much smaller than the band edge difference between the layers, which has only a minor effect on the band structure. However, in the VB, the SOC strength is larger than the band edge difference, resulting in four high-energy spin-split states at the band edges of the ±*K* valleys, displaying an alternating layer polarization pattern.[53,54] In the case of 2H-TMDs, without considering SOC, the CB in both the top and bottom layers are doubly generated at the ±*K* points due to inversion symmetry, with the bands splitting due to interlayer coupling. When SOC is included, the CB has a fourfold degeneracy, which is reduced twofold by band splitting (Figure 2b). Unlike 3R-TMDs, the CB spin states in 2H-TMDs retain their degeneracy under SOC owing to inversion symmetry; therefore, each energy state contains both up and down spins. In the VB, the SOC increases band-edge splitting with no spin polarization.[53]

For incommensurate ML-TMDs, lattice relaxation causes changes in the interlayer distance depending on the twist angle, which significantly affects the moiré bands. The twist angle in real space corresponds to a rotation in the momentum space, leading to a relative rotation of the Brillouin zones associated with each monolayer (Figure 2c). In this structure, the *K* points of each layer are slightly displaced, forming the two corners of the moiré Brillouin zone, denoted as $\kappa_{\pm}$. The band structures calculated using the continuum model approach showed a strong dependence on the twist angle (Figure 2d).[55,56] As the twist angle increases, the maximum and minimum of the VB top band shift from $\kappa_{\pm}$ to γ. Accordingly, the electronic band is flattened at a certain twist angle, called the "magic angle (θ_m)," where the band energies $\kappa_{\pm}$ and γ are consistent.[40,56–58] Near this angle, various electronic properties, such as the Mott insulating behavior, superconductivity, and fractional quantum anomalous Hall effect (FQAHE), have been observed in the fractional filling of the moiré unit cell.[41,59–66]

3.2. Exciton Characteristics

One of the unusual optical features of ML-TMDs is the formation of interlayer excitons and electron-hole pairs that are spatially separated due to differences in the CBM and VBM in each layer but strongly bound by Coulomb interactions between adjacent layers. The spatial separation between charges in the interlayer excitons creates a permanent electric dipole moment oriented along the out-of-plane direction, enabling electrical control over their optical and transport properties.[67–73] Exciton characteristics in commensurate 3R- and 2H-TMDs are largely governed by interlayer coupling, which varies significantly depending on stacking order. However, there are conflicting studies regarding that stacking configuration exhibits stronger interlayer coupling. Some studies have been reported that 2H-TMDs exhibit stronger interlayer coupling as evidenced by broader exciton linewidth and significant interlayer exciton absorption caused by hole delocalization across both layers.[74–77] In contrast, other studies have been reported that 3R-TMDs exhibit stronger interlayer coupling, highlighting higher charge carrier mobility and enhanced interlayer interactions.[54,78,79] However, it is commonly acknowledged that the cause of these characteristics is that inversion symmetry is broken in 3R-TMDs, resulting in a distinct excitonic transition.[54,74–80] In particular, it has been consistently observed that the intensity of the second harmonic generation signal is significantly higher in 3R-TMDs than in 2H-TMDs, which is attributed to the broken inversion symmetry.[54,76–79] Therefore, the study of interlayer coupling and exciton characteristics in commensurate ML-TMDs requires continuous research, as interpretations may vary depending on experimental conditions and material properties.

On the other hand, it has been reported recently that incommensurate ML-TMDs exhibit distinctive interlayer excitons, which are trapped in periodic potentials created by the moiré pattern, and referred to as moiré excitons.[81–88] The moiré pattern induces spatially varying local atomic registries, creating a periodic potential that traps excitons and can lead to their localization. Therefore, moiré excitons can be artificially controlled by structural adjustments using the twist angle, as demonstrated

by corresponding theoretical studies.[82,87–92] Three moiré exciton states, indicated as I, II, and III in Figure 2e, were observed in the WSe_2/WS_2 moiré superlattice with a near-zero twist angle by measuring the absorption characteristics using reflection-contrast spectroscopy.[81] These states disappear when the twist angle increases at a large twist angle of $\theta > 3°$. In addition, the $WS_2/MoSe_2$ hetero-bilayers show twist angle dependence, where the absorption energy blue-shifts as the twist angle approaches 30° from 0° or 60°, owing to the increased kinetic energy from the momentum of the moiré exciton.[82]

As the moiré pattern changes depending on the twist angle, the diffusion length and lifetime of the moiré excitons also change (Figure 2f). At a twist angle of 0°, the moiré potential is stronger than that at 60°, leading to a shorter exciton lifetime owing to the reduced diffusion length. As the twist angle increases, the moiré period decreases, and the momentum of the moiré excitons increases. Consequently, moiré excitons have longer lifetimes because their increased kinetic energy allows them to tunnel more easily between moiré supercells. Conversely, as the moiré period increases, exciton tunneling diminishes exponentially, resulting in localized moiré excitons and shorter lifetimes.[84,85]

For reconstructed ML-TMDs, on the other hand, atomic reconstruction leads to the formation of multiple ultraflat bands. Unlike the moiré potential of a rigid structure, which gradually modulates the band structure with mostly curved dispersion, the reconstructed system forms a modulating confining potential, effectively creating periodic quantum wells. This transformation results in an increased moiré potential depth, which enhances exciton localization.[40,90]

Studies on ML-TMDs over three layers have also been reported. Compared to twisted homo-bilayer TMDs, twisted homo-trilayer TMDs with the same twist angle exhibit an increased moiré potential depth. Additionally, as the twist angle increases, the moiré period decreases, similar to the twisted bilayer TMDs, leading to an increase in the moiré potential depth.[93] On the other hand, in twisted hetero-trilayer TMDs, it has been revealed that stacking a specific single-layer TMDs on top of a twisted hetero-bilayer TMDs can enhance PL by increasing light absorption and exciton population.[94] Furthermore, a study on four-layer twisted ML-TMDs with a twist angle between the two bilayers has been reported. Compared to the $1L\text{-}WSe_2/1L\text{-}WSe_2$ moiré superlattice, the moiré excitons in the $2L\text{-}WSe_2/2L\text{-}WSe_2$ moiré superlattice were more localized at the same twist angle, which is attributed to the encapsulation effect of the additional top and bottom WSe_2 monolayers.[95]

Valleytronics in ML-TMDs, meanwhile, has emerged as a promising platform for quantum information storage and optoelectronic applications due to its ability to control valley

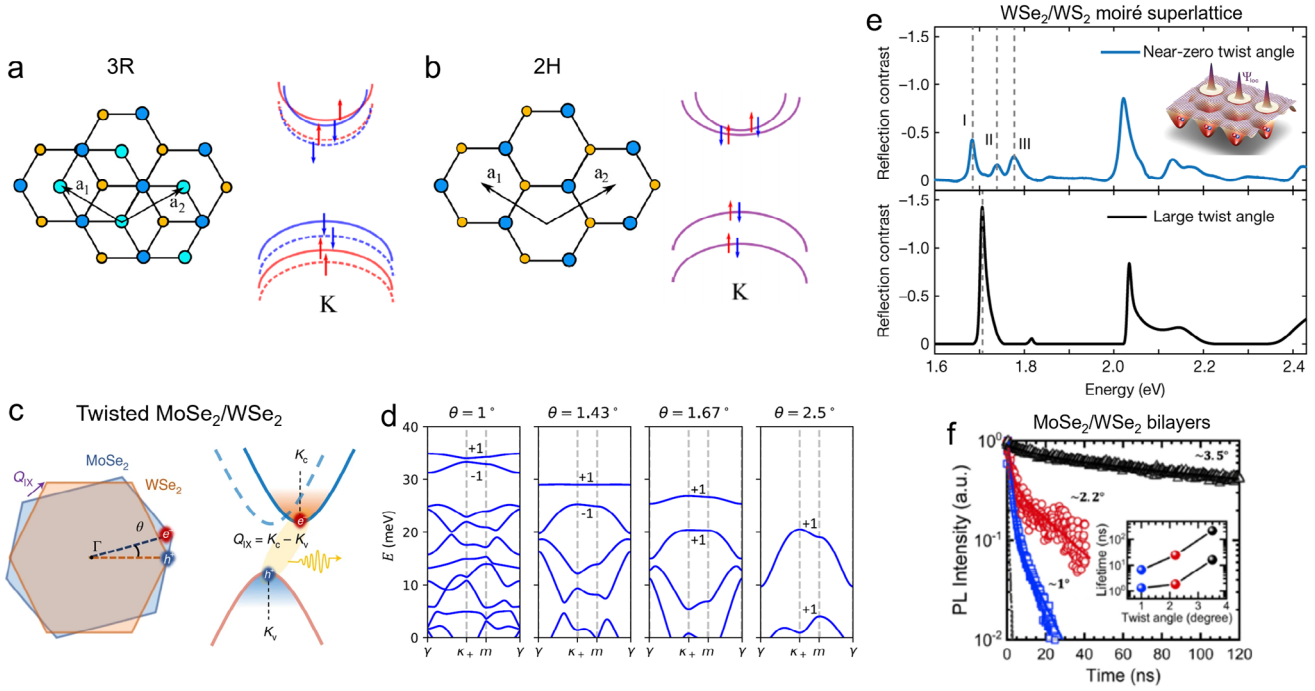

Figure 2. Schematics of the crystal and band structures with spin–orbit coupling of a) 3R and b) 2H bilayer MoS_2. a,b) are reproduced with permission.[53] Copyright 2018, American Physical Society. c) Schematics of the Brillouin zone of the twisted $MoSe_2/WSe_2$ heterostructure and the moiré band structure including indirect transition due to a finite momentum mismatch between the two layers. d) Emergence of flat bands depending on twist angle in twisted bilayer WSe_2, including calculated band structures along with the Chen numbers of the first two bands. Reproduced under terms of the CC-BY license.[56] Copyright 2021, Devakul et al., published by Springer Nature. e) Schematic of the moiré exciton (inset) and reflection contrast spectrum of the WSe_2/WS_2 moiré superlattice with three prominent peaks corresponding to distinct moiré exciton states. Reproduced with permission.[81] Copyright 2019, Springer Nature. The inset of e) is reproduced under the terms of the CC-BY license.[87] Copyright 2020, S. Brem et al., published by American Chemical Society. f) Twist angle dependence of the lifetime of a moiré exciton in three $MoSe_2/WSe_2$ bilayers with 1°, 2.2°, and 3.5° twist angles. The inset summarizes the extracted fast and slow decay components in the three twisted bilayer samples. c) and f) are reproduced with permission.[85] Copyright 2021, American Physical Society.

polarization through moiré potentials, interlayer coupling, and external fields. In twisted bilayers and hetero-bilayers, moiré superlattices create periodic potential landscapes that spatially modulate excitons, leading to enhanced valley polarization retention and prolonged exciton lifetimes.[96,97] The twist angle plays a crucial role in tuning valley properties, with small twist angles suppressing valley mixing and large twist angles facilitating valley-polarized free charge carrier transfer.[96] Additionally, interlayer excitons, formed by spatially separated electron-hole pairs across different layers, exhibit significantly longer lifetimes than intralayer excitons, making them ideal for valley information storage and manipulation.[98,99] External electric fields further allow precise tuning of valley dynamics by shifting interlayer exciton energies, enabling robust valleytronic memory and logic devices.[99] Moreover, magnetic fields can selectively align electron spins along valley axes, integrating spin and valley degrees of freedom for potential quantum applications.[100] These mechanisms position multilayer and twisted TMDs as a versatile platform for valley-based optoelectronics, offering potential breakthroughs in quantum computing, valleytronic memory, and tunable light-matter interactions.[101]

In summary, one of the unique optical properties of ML-TMDs is the formation of interlayer excitons, where electron-hole pairs are spatially separated between layers but remain strongly bound by Coulomb interactions, creating a permanent out-of-plane dipole moment that enables electrical control over their optical and transport properties.[67–73] In commensurate ML-TMDs, exciton characteristics are influenced by inversion symmetry in 3R- and 2H-TMDs, but conflicting reports on interlayer coupling strength necessitate careful evaluation of exciton properties.[54,74–80] In incommensurate ML-TMDs, moiré patterns generate periodic potentials that trap excitons, forming moiré excitons, whose properties can be tuned by adjusting the twist angle.[81–92] In reconstructed ML-TMDs, atomic reconstruction creates periodic quantum wells with ultraflat bands, enhancing exciton localization more effectively than a rigid moiré potential.[40,90] ML-TMDs with more than three layers also exhibit increased moiré potential depth and modified optical properties.[93–95] Furthermore, valleytronics has emerged as a promising platform for quantum information storage and optoelectronic applications by utilizing moiré potentials, interlayer coupling, and external fields to manipulate valley polarization, where small twist angles suppress valley mixing while large twist angles enhance valley-polarized charge carrier transfer, enabling tunable valleytronic functionality.[96–101] Consequently, the diverse exciton characteristics in ML-TMDs open new possibilities for next-generation quantum devices, high-performance optoelectronic components, and tunable light-matter interactions, positioning them as a versatile platform for advanced nanotechnology applications.

3.3. Carrier Mobility and Electrical Conductivity

In commensurate structures, electronic band structure differences according to the presence or absence of inversion symmetry cause the electrical characteristics to differ between stacking types. It has been reported that 3R-TMDs have a higher conductance than 2H-TMDs because of stronger interlayer coupling through band splitting originating from the absence of inversion symmetry (**Figure 3**a–c).[54] In addition, in the case of intralayer transport, there is no difference between the 2H- and 3R-TMDs, whereas in the case of interlayer transport, the 3R-TMDs have a lower interlayer resistance than the 2H-TMDs because of stronger interlayer coupling.

In incommensurate ML-TMDs, the charge-carrier mobility is highly sensitive to the twist angle.[96,102,103] At small twist angles, strong interlayer coupling and the formation of minibands in the moiré superlattice can localize charge carriers, significantly reducing their mobility. In this case, the flat bands in the moiré superlattice trap carriers in specific regions, limiting their movement and resulting in low mobility. As the twist angle increases, the miniband effects weaken, allowing the carriers to move more freely, and the mobility increases. At large twist angles, each layer behaves similarly to decoupled monolayers, where the mobility is primarily determined by the scattering mechanisms within each individual layer. For this reason, experimental results have been reported that mobility is higher at a twist angle of 30° compared to 0° in both bilayer and trilayer TMDs.[103]

Twisted ML-TMDs have recently gained significant attention owing to the emergence of novel quantum phenomena such as correlated electronic states, sparking active research into their diverse potential applications.[41,59–62,104] At the magic angle, the electronic band structure flattens, giving rise to flat bands. In these flat bands, the kinetic energy of the electrons is significantly reduced, causing the electrons to localize at specific lattice sites and allowing electron-electron interactions to dominate.[104] In a typical system, the kinetic energy of electrons is sufficiently high to allow them to move freely, whereas, in the flat bands formed at the magic angle, the reduced kinetic energy leads to stronger electron-electron correlations. These strong correlations are responsible for the Mott insulating behavior, a phase in which electrons, despite being present in sufficient numbers to conduct electricity, are unable to move freely because of the repulsive Coulomb interactions between them. This phenomenon is a hallmark of strongly correlated systems, where the traditional band theory cannot adequately explain the insulating behavior.

While the Mott insulating phase is an insulating state, it often serves as a precursor to superconductivity. Twisted bilayer graphene has a flat band at the magic angle (≈1.1°) and an insulating phase (Mott insulator) in the half-filling state. Furthermore, it was reported that twisted bilayer graphene has superconducting states over and below the half-filling carrier density with a Mott insulating state of $\theta = 1.16°$ below $T_c = 0.5$ K, as shown in Figure 3d,e.[62] The same phenomenon was observed in the flat band of twisted ML-TMDs. Twisted bilayer WSe_2 exhibited a Mott insulating state under a critical temperature (T_c) when half-filled near the magic angle of 4°–5.1°. In addition, an insulating response occurred in the half-filled 3.5°–5.1° twisted bilayer WSe_2 below 35 K, and superconducting behavior with zero resistance was observed in a state slightly off-half-filled below 3 K (Figure 3f,g).[41,63,105] Moreover, the superconductivity of twisted bilayer WSe_2 was observed by the supplementation of contacts, improved design of the dual-gated device, and reduced moiré inhomogeneity to ≈2–3% of the moiré density over a large channel area.[63] It was found that the superconductivity is observed in only the layer-hybridized region of the twisted bilayer and strongly confined near the filling factor of $\nu = 1$. In

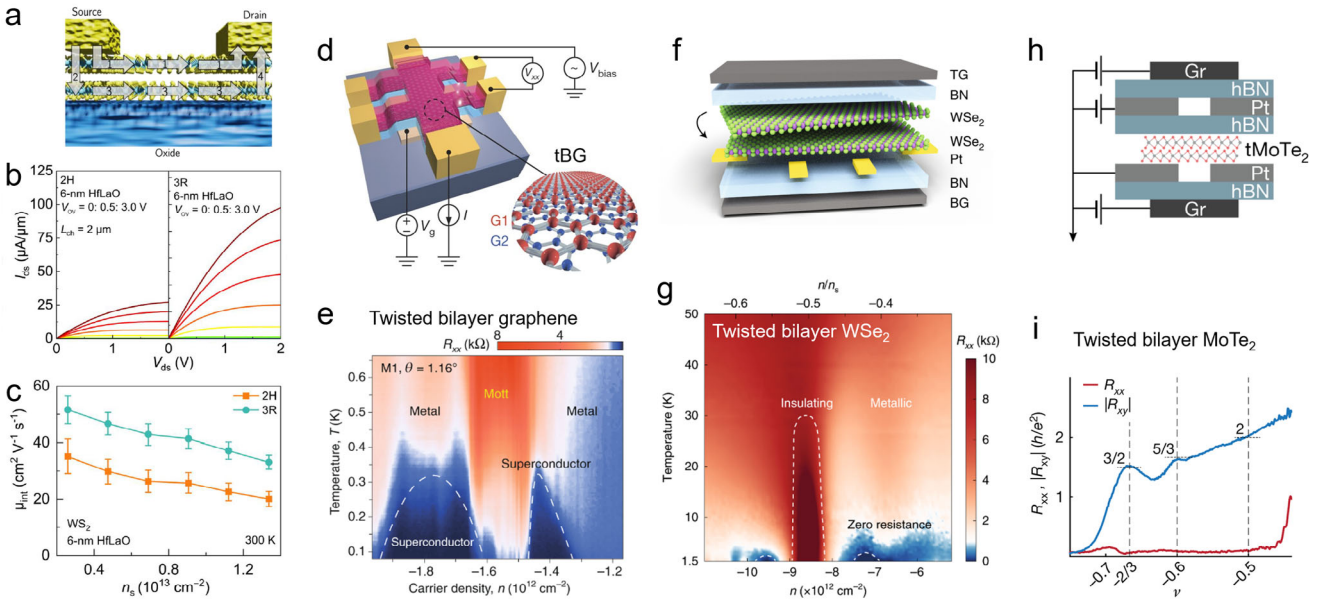

Figure 3. a–c) Electrical properties of commensurate ML-TMDs, a) Schematic of charge transfer in a 3R-bilayer TMDs device, b) Output characteristics, and c) effective mobility versus channel carrier density of a bilayer WS_2 FET with 2H and 3R stacking. a-c) are reproduced under the terms of the CC-BY-NC license.[54] Copyright 2023, Li et al., published by American Association for the Advancement of Science. d) Schematic of a twisted bilayer graphene device for four-probe measurement and e) four-probe resistance, R_{xx}, with two superconducting domes next to the half-filling state. d) and e) are reproduced with permission.[62] Copyright 2018, Springer Nature. f) Schematic of a twisted bilayer WSe_2 device and g) doping of two superconducting regions away from the insulating state. f) and g) are reproduced with permission.[41] Copyright 2020, Springer Nature. h) Schematics of a twisted bilayer $MoTe_2$ device for measuring the Hall resistance (R_{xy}), and i) fractionally quantized R_{xy}, which represents the FQAHE in twisted bilayer $MoTe_2$. h) and i) are reproduced with permission.[109] Copyright 2023, Springer Nature.

addition, a phenomenology distinct from that observed in graphene moiré systems was demonstrated, including a continuous transition from a superconductor to an insulator by tuning the external electric field and two nonspontaneous spin- or valley-polarized metallic states.

To summarize, in commensurate ML-TMDs, inversion symmetry affects electrical properties, with 3R-TMDs exhibiting higher conductance than 2H due to stronger interlayer coupling.[54] In incommensurate ML-TMDs, charge carrier mobility depends on the twist angle, decreasing at small angles due to miniband formation and increasing at larger angles as layers decouple.[96,102,103] At the range of the magic angle, band flattening enhances electron correlations, leading to Mott insulating and superconductivity.[41,59–62,104] The ability to control these quantum phases through twist angle engineering offers exciting opportunities for applications in quantum computing and other advanced technologies.[64–66,106] By adjusting the twist angle, researchers can explore the rich phase diagrams of twisted ML-TMDs, uncovering new correlated states and quantum effects that can be harnessed for future devices. The potential of twisted ML-TMDs for quantum information processing, high-performance computing, and unconventional superconductivity continues to drive research in this rapidly evolving field.

3.4. Anomalous Transport Behaviors

Twisted ML-TMDs exhibit the AHE, where a transverse voltage is generated in response to a longitudinal current even without an external magnetic field.[107–110] Unlike the ordinary Hall effect, which arises from the Lorentz force, the AHE is driven by Berry curvature, an intrinsic property of the electronic band structure that acts like an effective magnetic field in momentum space.[111,112] In twisted ML-TMDs, Berry curvature emerges due to moiré superlattice effects, strong spin–orbit coupling, and time-reversal symmetry breaking induced by internal magnetism or external perturbations.[111–114] The moiré superlattice modifies electronic bands, breaking spatial inversion symmetry and creating nontrivial Berry curvature distributions, while the strong spin–orbit interaction enhances valley-contrasting effects. When Berry curvature is present, charge carriers experience an anomalous velocity perpendicular to the applied electric field, leading to a transverse current as if they were moving in a real magnetic field.[115–118] This effect has been theoretically analyzed using first-principles electronic structure calculations such as density functional theory combined with Wannier function methods to extract Berry curvature and Chern numbers, as well as continuum models that provide an analytical approach to studying moiré bands and their topological properties.[56,110–120]

Beyond the AHE, the quantum AHE (QAHE) is a quantized version of the AHE, where the Hall resistivity becomes quantized in integer multiples of h/e^2, even in the absence of an external magnetic field. The QAHE is a manifestation of a topologically nontrivial electronic structure in which chiral edge states are protected by the topology of the system and contribute to dissipationless edge transport. These chiral edge states arise from the nonzero Chern number of the bulk bands, which is a topological invariant that characterizes the band structure.[110,121] The QAHE

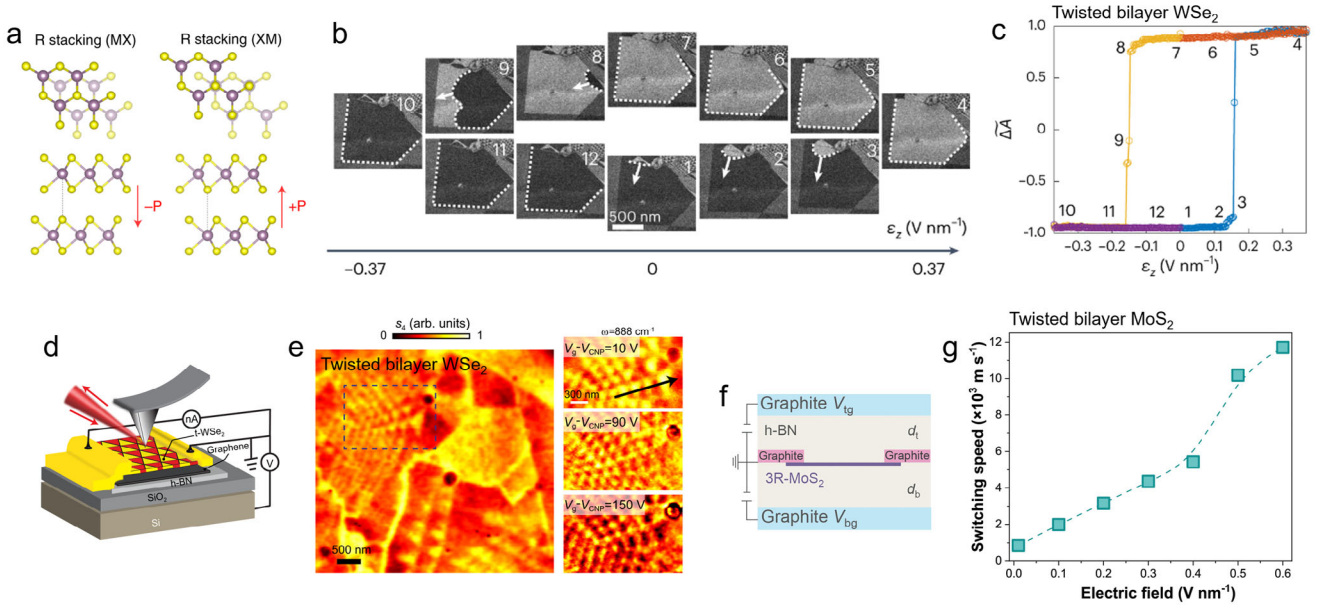

Figure 4. a) Schematics of polarization by R-type stacking configurations. a) is reproduced with permission.[125] Copyright 2022, Springer Nature. b) Snapshots of DF-TEM images, which represent the changes in polarization domains under a vertical electric field, and c) their corresponding normalized polarization $\widetilde{\Delta A}$ as a function of vertical electric fields, which represent the ferroelectricity of twisted bilayer WSe_2. b,c) are reproduced with permission.[128] Copyright 2023, Springer Nature. d) Schematics of a back-gated graphene device with a twisted WSe_2 bilayer on top and e) near-field scattering amplitude mapping of the device carried out with a photon energy of $\omega = 880$ cm^{-1} and $V_g - V_{CNP} = 10$ V, where V_{CNP} is the moiré-averaged charge neutrality. d) and e) are reproduced under the terms of the CC-BY license.[132] Copyright 2023, S. Zhang et al., published by Springer Nature. f) Schematics of a dual-gate bilayer 3R-MoS_2 device and g) average domain-switching speed with a varying electric field. f,g) are reproduced with permission.[133] Copyright 2024, American Association for the Advancement of Science.

characteristics have been observed in AB-stacked $MoTe_2/WSe_2$ moiré hetero-bilayers.[110] In contrast to the AA-stacking type, the QAHE state with broken time-reversal symmetry and nontrivial bands emerges by controlling the bandwidth and band topology by intertwining the moiré band with an electric field in the out-of-plane direction of each layer in the AB-stacked hetero-bilayer. Through this, in the zero magnetic fields, the Hall resistance (R_{xy}) is quantized to h/e^2 at filling factor $\nu = -1$ that is one hole per moiré unit cell and the longitudinal resistance (R_{xx}) vanishes. The AB-stacked $MoTe_2/WSe_2$ moiré hetero-bilayer was found to have a quantized Hall resistance of h/e^2 at low temperatures (≈2.5 K) in zero magnetic field. In addition, a Mott insulator-to-QAHE insulator phase transition was observed upon applying an external electric field.

A more exotic extension of the QAHE is the FQAHE, in which the Hall resistivity is quantized in fractional multiples of h/e^2. The FQAHE arises from strong electron–electron interactions in systems with topologically nontrivial band structures. In contrast to the integer QAHE, which is driven by a single-particle band topology, the FQAHE is a many-body phenomenon that requires the formation of strongly correlated states, such as fractional quantum Hall states, in the absence of an external magnetic field. ML-TMDs provide a promising platform for exploring the FQAHE owing to their tunable electronic interactions and potential for hosting strongly correlated electron phases. Large spin–orbit coupling and the possibility of inducing flat bands in TMDs heterostructures with a magic angle can enhance electron correlations, which are key components for realizing the FQAHE.[108,109,120,122] The FQAHE has been experimentally demonstrated in an AA-stacked twisted multilayer $MoTe_2$ (≈3.6°). At $\nu = -1, -\frac{2}{3}$, and $-\frac{3}{5}$ states, each has a fractionally quantized value of Hall resistance $R_{xy} = h/e^2$, $\frac{3}{2}h/e^2$, and $\frac{5}{3}h/e^2$, respectively (Figure 3h,i).[108,109,120]

In ML-TMDs, both the integer and fractional QAHE rely on the interplay between the topological band structures, magnetic ordering, and strong electron correlations. The tunability of TMDs properties through various external parameters, such as the electric field, strain, and doping, offers a unique opportunity to explore a wide range of quantum phases and topological phenomena. As the field of 2D materials continues to grow, ML-TMDs are likely to play a central role in the study of QAHE, providing new insights into both fundamental physics and potential technological applications.

3.5. Sliding Ferroelectricity of Reconstructed ML-TMDs

Vertical ferroelectric switching occurs via in-plane interlayer sliding without vertical ion displacement in reconstructed ML-TMDs with multiple domains.[123–131] In 2H-stacked ML-TMDs, alternating metal and chalcogen layers preserve the inversion symmetry and suppress ferroelectricity. In contrast, noncentrosymmetric stacking induces out-of-plane polarization, which enables ferroelectricity. In the case of 3R-stacked twisted bilayer TMDs, the MMXX domains are non-polarized, and the MX and XM domains are polarized in the opposite direction (**Figure 4a**), leading to zero total vertical polarization owing to the same distribution of domains. The MX (XM) domains have a downward (upward)

polarization because of the vertical alignment of faced M and X atoms. These domains exist alternately according to the moiré period, which is known to change the distribution of domains under an external electric field. Therefore, the total polarization of the 3R phase can be modulated via interlayer translation using an external electric field. Unlike 3D ferroelectric materials that have a depolarization field at the interface between the TMDs and the substrate, the clean vdW interface in the 3R-TMDs bilayers further enhances polarization and causes the layer to slide through an external electric field, resulting in polarization reversal.[123–131]

Real-time external field-dependent changes in the MX and XM domains have been observed using operando dark-field transmission electron microscopy (DF-TEM) (Figure 4b,c) to reveal the correlation between domain morphology and sliding ferroelectricity.[128] When a vertical electric field is applied parallel (antiparallel) to the polarization direction of the MX (XM) domains, the stacking energy of the MX (XM) domains became lower than that of the XM (MX) domains. This stacking energy difference acts as a driving force for the domain transition through atomic sliding, leading to a change in the ratio of the MX and XM domains and a large hysteresis owing to the dynamics of the domain wall motion and their interaction with the pinning sites in the material (Figure 4b,c). Piezoresponse force microscopy (PFM) and Kelvin probe force microscopy have been employed to investigate the electromechanical surface deformation and electrostatic force in 3R-type polydomain bilayer TMDs, respectively.[124,125] It has also been reported that the ferroelectric moiré domains can be visualized through near-field infrared (NFI) nanoimaging by imprinting polarization in the moiré domains on the plasmonic response of graphene (Figure 4d,e).[132]

Recently, the potential for creating fatigue-free ferroelectric devices using the sliding ferroelectricity of twisted bilayer 3R-MoS_2 has been demonstrated (Figure 4f,g).[133] This 2D ferroelectric device exhibited neither a wake-up effect at low cycles nor significant fatigue, even after 10^6 switching cycles under varying pulse widths. Moreover, the device showed a total stress time of up to 10^5 s under an electric field and an ultrafast switching speed of ≈0.3 ns for a 1000 nm-diameter domain. However, challenges remain regarding the controllability of domains, long-term stability, selective switchability, and scalability. Nevertheless, we expect that the sliding ferroelectricity of ML-TMDs can provide platforms for non-volatile memory and potential applications through further in-depth research.

4. Fabrication of ML-TMDs

Various methods, such as the mechanical stacking of exfoliated flakes and chemical synthesis, have been used to produce ML-TMDs with commensurate or incommensurate structures. The most representative method for fabricating ML-TMDs with a desired twist angle is the tear-and-stack method using mechanically exfoliated TMDs flakes.[134–136] In this process, a polymer-coated elastomer stamp is used to partially pick up and tear an exfoliated TMDs flake. Subsequently, rotation is performed at the desired angle and then transferred to the remaining flake to produce the multilayer 2D material.[135,136] However, this method limits the size of fabricated ML-TMDs. By applying this method, a combined method of epitaxial growth and the tear-and-stack technique has been employed for the large-area fabrication of twisted ML-TMDs.[103] First, MoS_2 is epitaxially grown on a *c*-sapphire substrate using chemical vapor deposition (CVD) and then cut into a constant rectangular size. Second, twisted ML-TMDs with a specific twist angle is fabricated by transferring the TMDs film onto the other using PDMS (**Figure 5**a,b). However, the fabrication of wafer-scale twisted ML-TMDs using this method is challenging.

Therefore, considerable efforts have been devoted to directly synthesizing commensurate and incommensurate ML-TMDs.[137–139] The 2H and 3R phases of TMDs can be selectively grown by CVD through the precise control of the growth temperature, as shown in Figure 5c,d.[137] After single-layer MoS_2 is grown at 700 °C, the second layer of MoS_2 is grown at higher temperatures of 750 and 800 °C. Bilayer MoS_2 with stacking type of 3R and 2H is synthesized at 750 and 800 °C, respectively. A higher second-step growth temperature reduces the wettability of the substrate, leading to the growth of a second layer on top of the monolayer. Furthermore, the stacking type is determined by the second-step growth temperature, as the free energy of the 2H phase becomes lower than that of 3R with increasing temperature. In addition, remote epitaxy was proposed to grow R-stacked ML-TMDs on *a*-plane sapphire because the stacking configuration of R-stacked bilayer WS_2 is more energetically favorable across the atomic steps of *a*-plane sapphire than that of the H-stacked ones.[138] With the increasing interest in twisted bilayer TMDs, a synthesis method involving the direct CVD growth of twisted bilayer TMDs with various twist angles has been proposed, as shown in Figure 5e,f.[139] When a NaCl promoter was used, bilayer MoS_2 with different twist angles was fabricated. However, this method makes it difficult to achieve only the desired twist angle, and the distribution of twist angles follows a Gaussian distribution.

The growth of single-crystalline commensurate ML-TMDs is important because multilayers provide another opportunity to control the band structures and electrical properties of the same TMDs through thickness. Step-guided growth was demonstrated for uniformly aligned ML-TMDs on stepped sapphire surfaces.[140,141] The thickness of ML-TMDs can be controlled by controlling the step height of the sapphire surface, guiding the simultaneous nucleation of ML-TMDs with aligned edges, and promoting the continuous growth of ML-TMDs films. In addition, it has been demonstrated that 3R-TMDs can be grown at the interface between Ni and TMDs with thickness control by utilizing the diffusion of metal and chalcogen species through a single-crystalline Ni foil, as depicted in Figure 5g, which is called interfacial epitaxy. On the Ni surface, the precipitated metal and chalcogen atoms formed aligned MX_2 nuclei and grew into unidirectionally oriented single-crystal 3R-TMDs.[142] The hypotaxy method was suggested as a synthetic method for fabricating single-crystalline ML-TMDs, as depicted in Figure 5h.[143] Hypotaxy is the downward growth of single-crystal ML-TMDs under the guidance of a graphene template placed on top of a transition metal film via chalcogenization. This method enables the fabrication of single-crystal ML-TMDs with precise thickness control on various substrates.

Various fabrication methods for ML-TMDs continue to be actively explored. However, to enhance the practical feasibility of ML-TMDs for various applications, the development of wafer-scale synthesis techniques is essential. In the case of

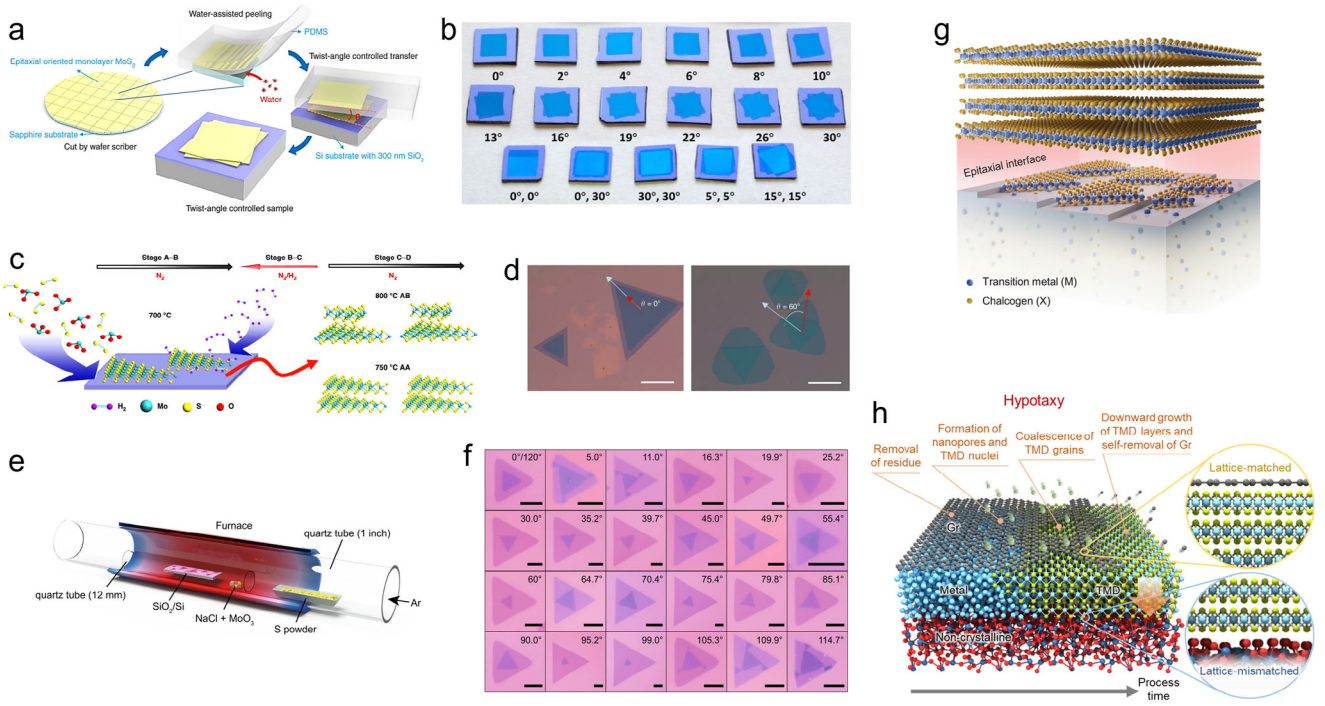

Figure 5. a) Tear-rotate-stack method using epitaxially grown TMDs and b) images of twist angle-engineered multilayer MoS_2. a) and b) are reproduced under the terms of the CC-BY license.[103] Copyright 2020, Liao et al., published by Springer Nature. c) Schematic and d) optical images of the temperature dependence of the stacking configurations in the reverse-flow chemical vapor epitaxy process for bilayer MoS_2. c,d) are reproduced under the terms of the CC-BY license.[137] Copyright 2019, Zhang et al., published by Springer Nature. e) Schematic of the CVD set up for the direct synthesis of twisted bilayer MoS_2 using NaCl promoter and f) optical images of the grown samples. e) and f) are reproduced under the terms of the CC-BY license.[139] Copyright 2024, Xu et al., published by Springer Nature. g) Schematics of interfacial epitaxy in single crystalline ML-TMDs growth. Reproduced with permission.[142] Copyright 2024, American Association for the Advancement of Science. h) Schematic of the growth mechanism of hypotaxy in single crystalline ML-TMDs growth. Reproduced with permission.[143] Copyright 2025, Springer Nature.

commensurate ML-TMDs, several recent studies have demonstrated fabrication methods that allow precise layer number control at the wafer scale.[141–143] In contrast, for incommensurate ML-TMDs, research on wafer-scale synthesis techniques that achieve a desired twist angle remains extremely limited. Since transfer techniques inherently impose size constraints, a completely new synthetic approach is required to realize these structures without relying on post-synthesis stacking.

5. Potential and Applications of ML-TMDs

ML-TMDs exhibit unique electrical and physical properties owing to their interlayer interactions, making them promising materials for next-generation devices. Key characteristics, such as the layered structure, interlayer excitons, and ferroelectricity, have attracted significant attention for applications ranging from enhancing traditional devices, such as FETs, to developing novel prototypes. In this section, we highlight the potential of ML-TMDs to overcome the limitations of monolayers and offer insights for future research.

5.1. Device Applications of Commensurate ML-TMDs

Early research on the applications of ML-TMDs mainly focused on utilizing the layer-dependent properties of commensurate ML-TMDs structures with 2H and 3R. The electrical and physical properties of ML-TMDs vary depending on the number of layers, making it crucial to select the appropriate layer count for enhanced device performance. A notable example is the vertical tunnel FET (TFET), which utilizes a layered structure to overcome the performance limitations of conventional FETs (**Figure 6a**). In this device, band-to-band tunneling (BTBT) occurs in the out-of-plane direction of the ML-TMDs channel, surpassing the thermionic limitation of the subthreshold swing.[144] The tunneling barrier width of the channel can be tuned by adjusting the number of layers of the ML-TMDs to achieve superior switching performance. Bilayer MoS_2 provided a sufficiently low tunneling barrier width while preventing leakage current, enabling the realization of a sub-thermionic subthreshold swing with ≈31.1 mV dec^{-1} at room temperature (Figure 6b). The bilayer channel also offers the advantages of a higher density of states and strong resistance to interface scattering compared with a monolayer.[73]

In specific TMDs such as WSe_2 and WS_2, the mobility difference between electrons and holes varies with the number of layers, leading to a shift in the dominant carrier type.[145] This suggests that the diverse transport behaviors of n-, p-, and ambipolar types can be induced in the same 2D channel by simply manipulating the number of layers. Ambipolar conduction with a high on/off current ratio can be used

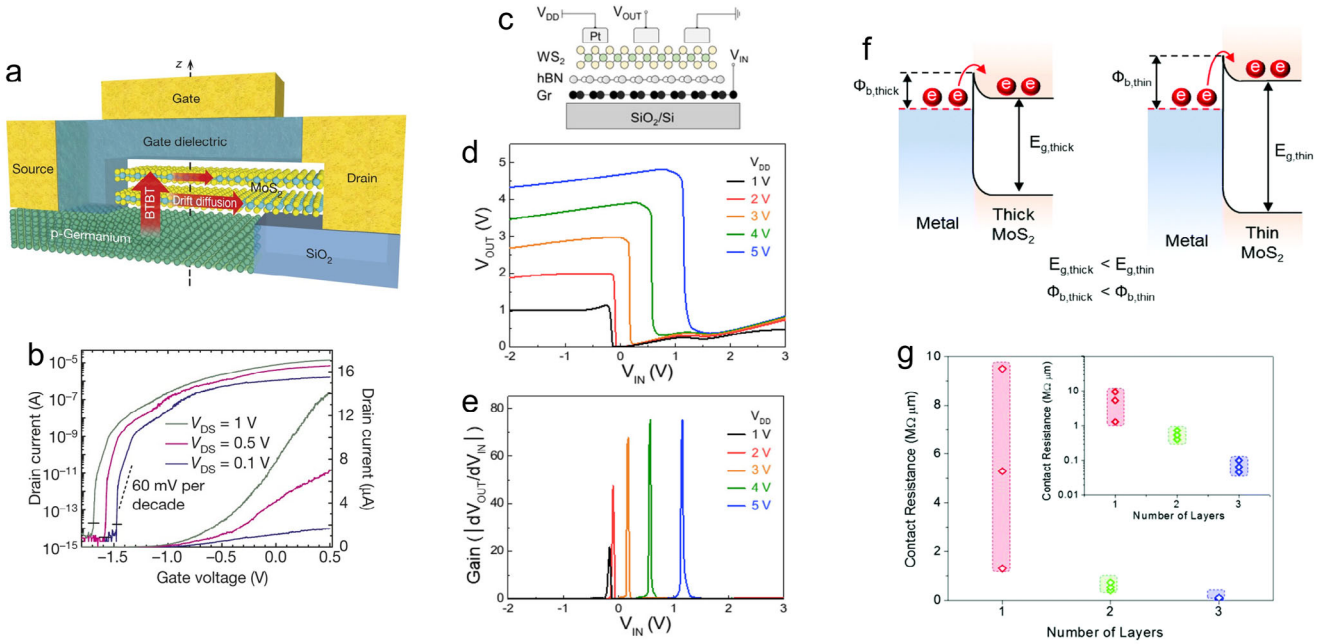

Figure 6. a) Schematic of the TFET with a bilayer MoS_2 channel and b) transfer characteristics showing subthermionic subthreshold swing (<60 mV dec^{-1}) at three distinct drain voltages (V_{DS}). a) and b) are reproduced with permission.[144] Copyright 2015, Springer Nature. c) Schematic of the CMOS-like 2D inverter utilizing a 12 nm-thick ambipolar WS_2 channel, along with its d) voltage transfer curves and e) corresponding gain characteristics (V_{IN}: input voltage, V_{OUT}: output voltage, V_{DD}: supply voltage). c–e) are reproduced with permission.[146] Copyright 2020, American Chemical Society. f) Energy band diagram of MoS_2 with different thicknesses at the metal contact interfaces ($\Phi_{b,thick}$, $\Phi_{b,thin}$, $E_{g,thick}$, $E_{g,thin}$: SBHs and energy bandgaps of thick and thin MoS_2). g) Layer-dependent contact resistance of MoS_2 FETs (inset: log scale). f) and g) are reproduced with permission.[147] Copyright 2017, The Royal Society of Chemistry.

to fabricate reconfigurable logic devices. Ambipolar ML-TMDs can be reversibly switched between n- and p-type conduction via electrostatic control, allowing for a single-channel configuration without the need for extrinsic doping. This capability simplifies the fabrication process, reduces costs, and provides significant advantages for device miniaturization. A complementary metal–oxide–semiconductor (CMOS)-like inverter has been successfully implemented using a single ML-WS_2 channel (12 nm-thick) with ambipolar conductance, achieving a notable gain of 78 without extrinsic doping, as shown in Figure 6c–e.[146]

The layer-dependent bandgap of TMDs can be used to reduce the contact resistance of metal electrodes and introduce diverse functionalities into 2D devices. By adjusting the number of layers in the ML-TMDs channel, the band alignment between the ML-TMDs and metal electrode can be optimized to lower the Schottky barrier height (SBH) at the contact region (Figure 6f).[147] A smaller SBH in thicker TMDs reduces the contact resistance and increases the carrier mobility, ultimately enhancing the operating speed and power efficiency of the device. Trilayer MoS_2 channel exhibited much smaller contact resistance by two orders of magnitudes compared to the monolayer in MoS_2 devices with Al contacts (Figure 6g). By combining the TMDs channel with different layer numbers in the source and drain regions, a rectifier consisting of the same TMDs can be realized owing to the difference in the SBH between the two electrodes.[148] This diode-like behavior can be exploited to fabricate high-performance optoelectronic devices, such as photodetectors and photovoltaic cells.

The ability to control transport properties by varying the number of layers optimizes device performance while maintaining compatibility with existing semiconductor technologies.[144,146–148] This intrinsic tunability allows ML-TMDs-based devices to overcome conventional material limitations, enhancing their potential for integration into advanced electronics. Future studies should extend the investigation of layer-dependent transport to incommensurate and reconstructed ML-TMDs to further clarify their electronic properties. A comprehensive understanding of these effects will be critical for expanding the applicability of ML-TMDs in nanoelectronics.

5.2. Optoelectronic Applications of Interlayer Excitons

In contrast to monolayer TMDs with only intralayer excitons, ML-TMDs exhibit both intralayer and interlayer excitons. Interlayer excitons, characterized by the spatial separation of electrons and holes in different layers, exhibit distinctive properties such as strong binding energy, prolonged lifetime, and tunable dipole moment. These unique characteristics suggest the possibility of developing interlayer exciton-based optoelectronic devices. Although these are still in the primary stages, several studies have reported the implementation of advanced optoelectronic devices using interlayer excitons.[149–153]

Excitonic devices are advanced optoelectronic systems that include exciton transistors and exciton diodes, which can be used for information processing by controlling the transport of

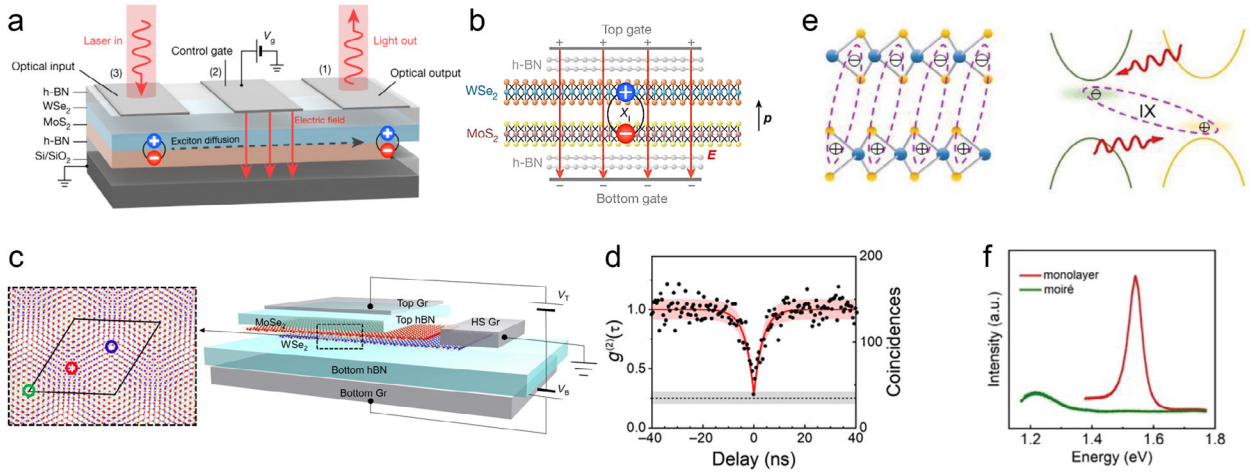

Figure 7. Schematic of a) excitonic transistor based on a WSe_2/MoS_2 hetero-bilayers and b) interlayer exciton with an out-of-plane dipole moment (p) whose flow can be controlled by an external electric field (E). a) and b) are reproduced with permission.[149] Copyright 2018, Springer Nature. c) Schematic of a single quantum emitter composed of $MoSe_2/WSe_2$ hetero-bilayers with a moiré pattern. d) Second-order correlation function showing a $g^{(2)}(0)$ value of 0.28 that demonstrates photon antibunching from moiré-trapped interlayer excitons. c) and d) are reproduced under the terms of the CC-BY license.[151] Copyright 2020, Baek et al., published by American Association for the Advancement of Science. e) Schematic showing the formation of a moiré miniband and the spatial separation of electrons and holes in multilayer $MoSe_2$ with a moiré pattern. f) Comparison of the PL spectrum between monolayer and multilayer $MoSe_2$ with a moiré superlattice, demonstrating strong interlayer interactions induced by the moiré structure. e) and f) are reproduced with permission.[153] Copyright 2024, Wiley-VCH.

excitons. Among the different types of excitons, interlayer excitons have excellent potential for implementation in low-loss exciton transistors owing to their long-range transport based on their prolonged lifetime. The control of the interlayer exciton flow over a micrometer-scale distance has been demonstrated in the MoS_2/WSe_2 heterostructure (**Figure 7a**).[149] In addition to the spatial separation of electrons and holes in individual layers, the heterojunctions of different TMDs show indirect transitions of interlayer excitons owing to the lattice mismatch and twist angle, leading to a reduced recombination rate and extended lifetime of interlayer excitons. Three control gates were positioned along the exciton diffusion pathway, and an electric field was applied in the out-of-plane direction of the channel to modulate the energy profile of exciton transport. When no electric field was applied to the control gate, interlayer excitons generated at the input region by laser irradiation showed a long diffusion distance of 3 µm, resulting in electron-hole recombination and light emission at the output region. In contrast, when a voltage was applied to the control gate, an energy barrier was formed in the exciton diffusion pathway, effectively hindering exciton transport (Figure 7b). Similarly, controlling the interlayer exciton diffusion was also demonstrated in WSe_2 homo-bilayers.[150]

The possibility of utilizing interlayer excitons as a single quantum emitter was demonstrated in twisted ML-TMDs with a moiré superlattice.[151] Tuning the twist angle between the $MoSe_2$ and WSe_2 layers formed a moiré pattern that confined the interlayer excitons within the moiré potential, resulting in photon antibunching (Figure 7c,d). Photon antibunching is a phenomenon in which photons from light emitters are separated individually, indicating that the moiré-trapped interlayer excitons are true single-quantum emitters. The low second-order correlation function $g^{(2)}(0)$ of 0.28 indicates that photon antibunching occurs in twisted $MoSe_2/WSe_2$ (Figure 7d). Such a single quantum emitter has the potential to implement a qubit, which is the basic unit of quantum information processing and is important for quantum communication and computing.[152] Precise control over the size and period of the moiré potential provides a uniform environment for interlayer excitons, making ML-TMDs an ideal platform for quantum emitter arrays.

ML-TMDs offer significant potential for enhancing the performance of traditional optoelectronic devices, particularly for extending their detection ranges. Although monolayer TMDs are generally limited in infrared light detection owing to their large bandgap, multilayer $MoSe_2$ with a moiré structure has successfully extended the detection range to the near-infrared (NIR) region.[153] The strong interlayer coupling in the moiré superlattice generates moiré minibands and spatially confines electrons and holes in different layers, enabling effective NIR detection (Figure 7e). The PL peak of the interlayer excitons further confirms the strong interlayer coupling in the moiré structure (Figure 7f).

Interlayer excitons in ML-TMDs provide a unique platform for controlling optical and electronic properties at the nanoscale. Their spatially separated charge carriers enable long exciton lifetimes and strong dipole interactions, which are crucial for advanced optoelectronic applications.[149–153] Recent progress in moiré superlattices has expanded the ability to control interlayer exciton behavior through twist angle engineering. Further advancements in scalable synthesis and stacking precision will be essential for improving device performance and stability in commercial applications.

5.3. 2D Ferroelectric-Based Applications

The switchable polarization of 2D ferroelectric materials has great potential for use in next-generation non-volatile memory and low-power devices. Two types of 2D ferroelectric devices

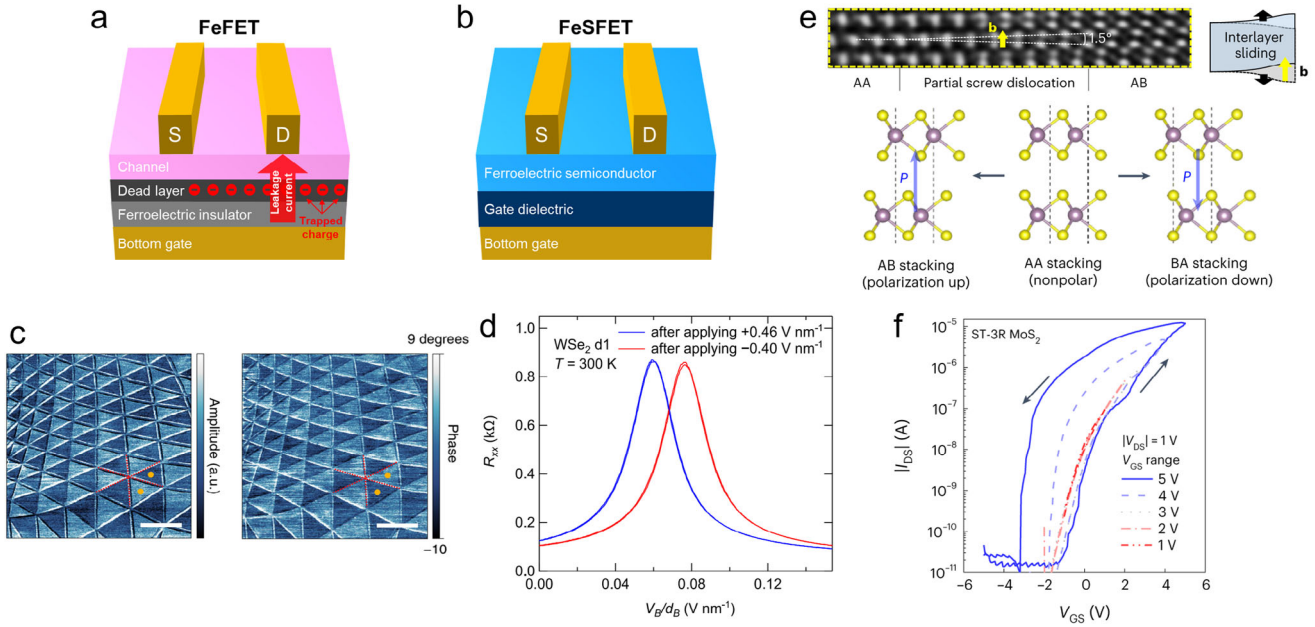

Figure 8. Schematic comparison of the device structures of a) FeFET and b) FeSFET, where FeSFET allows the integration of high-quality insulators, reducing gate-leakage current and charge trapping at the interface. c) Amplitude and phase images from vertical PFM on 0.25° twisted bilayer $MoSe_2$ (orange dots: triangular domains, red dotted lines: domain walls, scale bars: 200 nm). d) Ferroelectric hysteresis of a graphene-channel sensor, observed after applying opposite electric fields to the bottom gate, induced by domain wall motion in R-stacked bilayer WSe_2 serving as a ferroelectric insulator. (R_{xx}: resistance of the graphene channel, V_B: bottom gate voltage, d_B: thickness of the bottom dielectric). c) and d) are reproduced with permission.[125] Copyright 2022, Springer Nature. e) Schematic of the spontaneous shear transformation in epitaxial 3R bilayer MoS_2, along with a TEM image showing the partial screw dislocation. f) Ferroelectric hysteresis observed in the transfer curves of shear-transformed 3R MoS_2 FET under different gate voltage sweep ranges (V_{GS}: gate voltage, V_{DS}: drain voltage, I_{DS}: drain current). e) and f) are reproduced with permission.[127] Copyright 2023, Springer Nature.

exist: ferroelectric FETs (FeFETs) and ferroelectric semiconductor FETs (FeSFETs). In FeFETs, 2D ferroelectric materials are used as the gate dielectrics, as shown in **Figure** 8a. The polarization direction of the gate dielectric can be manipulated using an electric field, which modulates the conductivity of the semiconductor channel. Although the use of TMDs has been confined to the channel and conventional ferroelectric materials have been employed as dielectrics, recent studies have revealed that twisted ML-TMDs with polydomains can be used as ferroelectric insulators.[125,154] In contrast, a 2D ferroelectric semiconductor can be used as the channel for FeSFETs, as shown in Figure 8b. FeSFETs alleviate the constraints on selecting insulator materials such that conventional high-quality insulators can be used, offering benefits in terms of gate-current leakage and trapped charge at the interface.[155] Unlike conventional ferroelectrics, ML-TMDs with weak vdW interactions exhibit ferroelectricity through interlayer shear motion, resulting in a lower switching barrier and faster switching speed (Figure 4g). This unique mechanism enables FeSFETs to operate at lower voltages while maintaining stable polarization states, reducing the high power consumption associated with conventional ferroelectric dielectrics. Additionally, the absence of dangling bonds on the surface of ML-TMDs facilitates the formation of atomically sharp interfaces, minimizing defects that typically degrade device performance in conventional ferroelectric thin films.[156,157]

The ferroelectricity in ML-TMDs is closely related to the breaking of stacking symmetry.[125] In a twisted WSe_2/WSe_2 homobilayer with an R-stack, two triangular domains of MX (downward polarization) and XM (upward polarization) have been detected using PFM (Figure 8c). An external electric field can modulate the net polarity through the movement of the domain walls, enabling polarization switching. When a graphene sensor was placed on top of the twisted WSe_2/WSe_2 homo-bilayer, it exhibited robust ferroelectric hysteresis at room temperature (Figure 8d), indicating its suitability for non-volatile memory applications.

The fabrication of a FeSFET consisting of epitaxially grown 3R-type ML-TMDs channels was recently demonstrated. Spontaneous shear transformation induced ferroelectricity in the 3R MoS_2 epilayers.[127] The dominant AA phase (nonpolar) in the CVD-grown 3R MoS_2 epilayers spontaneously transformed into the AB (upward polarization) or BA phases (downward polarization) owing to energetic instability (Figure 8e). This transition also induces the formation of mobile partial dislocations within the 3R MoS_2 channel, enabling reversible polarity switching through interlayer sliding under an applied electric field. This process triggers charge redistribution between the layers and modulates the net polarity. The hysteresis loop in the I–V curve of the MoS_2 FeSFET increased in proportion to the gate voltage sweep range (Figure 8f). The MoS_2 FeSFET showed a data retention time exceeding 10^4 s and an endurance surpassing 10^4 cycles. In non-volatile memory applications, the stability of repeated polarity switching and resistance to fatigue are critical performance factors. This exceptional reliability originates from the vdW interaction between layers in ML-TMDs, which enables sliding ferroelectricity with a relatively low energy barrier. As a

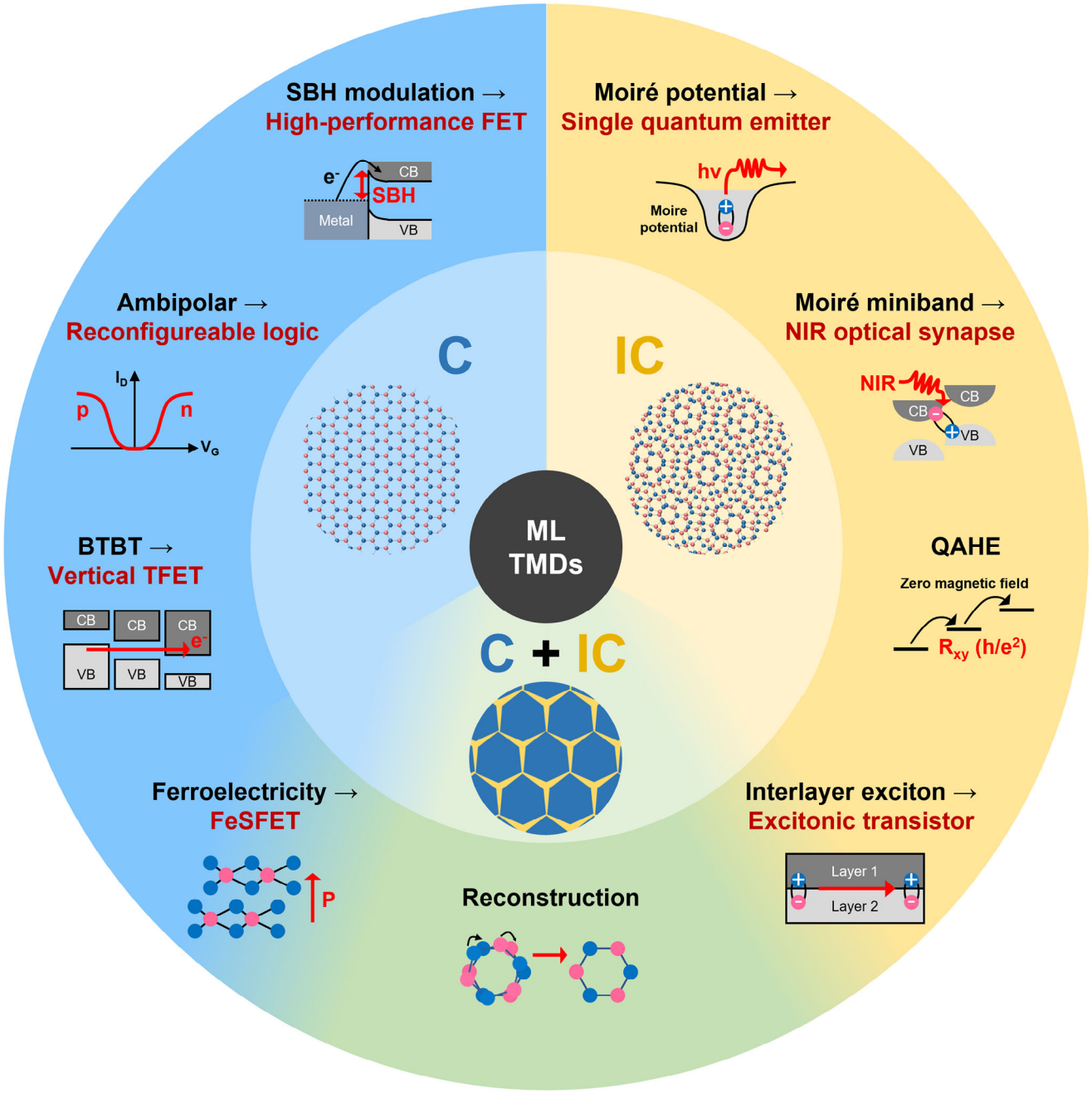

Figure 9. Structural classification of ML-TMDs, highlighting their diverse properties and potential applications.

result, polarization switching can be achieved at lower electric fields compared to conventional ferroelectrics, reducing power consumption while minimizing the fatigue effect.[156,157] Additionally, epitaxially grown MoS_2/WS_2 hetero-bilayers showed ferroelectricity in both 2H- and 3R-like configurations owing to symmetry breaking by different upper and lower layers.[158] The applied electric field of >2.4 V nm^{-1} induced a lateral sliding of 1.83 Å between the layers, leading to charge redistribution and polarization inversion. In this MoS_2/WS_2 hetero-bilayer, polarity switching has been applied to ferroelectric tunnel junction devices, which have emerged as a promising technology for nonvolatile memory.

Sliding ferroelectricity in ML-TMDs offers a novel platform for next-generation low-power memory technologies.[125,127,154–158] Their vdW interfaces allow robust polarization switching without the constraints of conventional ferroelectrics. Recent advances in stacking engineering have enhanced ferroelectric stability and tunability in these materials. Further research should focus on optimizing device architectures and scaling up fabrication techniques to enable practical applications.

6. Conclusion and Outlook

ML-TMDs exhibit unique properties arising from interlayer interactions such as bandgap engineering, moiré minibands, and correlated electronic states that are unattainable in monolayers. These properties, dictated by factors such as stacking order, twist angle, and number of layers, have enabled significant advancements in applications ranging from vertical TFETs to quantum devices leveraging moiré superlattices. Although mechanical stacking offers precise control over twist angles, its scalability is limited. In contrast, CVD enables large-area synthesis but lacks fine-angle control, highlighting the need for improved synthesis methods. For the scalable fabrication of ML-TMDs with controlled twist angles, integrating the advantages of both mechanical stacking and CVD has been considered as a potential approach. A promising strategy involves growing TMDs on substrates that facilitate single-crystalline growth, followed by wafer-scale transfer techniques to precisely control the twist angle.[159–162] **Figure 9** summarizes the structural classifications, optoelectronic properties, and diverse potential applications.

The ability to precisely engineer the interlayer interactions in ML-TMDs provides significant opportunities for enhancing device performances and developing novel device architectures. Although research on ML-TMDs is still in its early stages, a deeper understanding of the mechanisms governing interlayer interactions is critical. Moreover, the development of scalable synthesis methods capable of accurately controlling the interlayer angles without compromising material quality is essential. As this field advances, ML-TMDs are well-positioned to drive innovation in next-generation electronic and optoelectronic applications, establishing themselves as foundational elements for future nanotechnology.

Acknowledgements

H.G.O. and Y.Y. contributed equally to this work. This work was supported by the Technology Innovation Program (RS-2023-00301731 and RS-2023-00267003) funded by the Ministry of Trade, Industry & Energy (MOTIE), the National Research Foundation (NRF) (No. RS-2024-00401234 and RS-2024-00418210). G.H. Lee acknowledges the support from the Creative-Pioneering Researchers Program through Seoul National University (SNU), the Research Institute of Advanced Materials (RIAM), Institute of Engineering Research (IER), Institute of Applied Physics (IAP), SOFT Foundry Institute and the Inter-University Semiconductor Research Center (ISRC) at the Seoul National University.

Conflict of Interest

The authors declare no conflict of interest.

Keywords

commensurate, incommensurate, moiré structure, multilayer, reconstructed structure, transition metal dichalcogenides

Received: December 28, 2024
Revised: February 25, 2025
Published online: March 19, 2025

[1] S. Manzeli, D. Ovchinnikov, D. Pasquier, O. V. Yazyev, A. Kis, *Nat. Rev. Mater.* **2017**, *2*, 17033.
[2] Q. H. Wang, K. Kalantar-Zadeh, A. Kis, J. N. Coleman, M. S. Strano, *Nat. Nanotechnol.* **2012**, *7*, 699.
[3] S. Joseph, J. Mohan, S. Lakshmy, S. Thomas, B. Chakraborty, S. Thomas, N. Kalarikkal, *Mater. Chem. Phys.* **2023**, *297*, 127332.
[4] P. Zhao, J. Yu, H. Zhong, M. Rösner, M. I. Katsnelson, S. Yuan, *New J. Phys.* **2020**, *22*, 083072.
[5] B. Radisavljevic, A. Radenovic, J. Brivio, V. Giacometti, A. Kis, *Nat. Nanotechnol.* **2011**, *6*, 147.
[6] C.-H. Lee, G.-H. Lee, A. M. van der Zande, W. Chen, Y. Li, M. Han, X. Cui, G. Arefe, C. Nuckolls, T. F. Heinz, J. Guo, J. Hone, P. Kim, *Nat. Nanotechnol.* **2014**, *9*, 676.
[7] H. Wang, L. Yu, Y. H. Lee, Y. Shi, A. Hsu, M. L. Chin, L. J. Li, M. Dubey, J. Kong, T. Palacios, *Nano Lett.* **2012**, *12*, 4674.
[8] G. R. Bhimanapati, Z. Lin, V. Meunier, Y. Jung, J. Cha, S. Das, D. Xiao, Y. Son, M. S. Strano, V. R. Cooper, L. Liang, S. G. Louie, E. Ringe, W. Zhou, S. S. Kim, R. R. Naik, B. G. Sumpter, H. Terrones, F. Xia, Y. Wang, J. Zhu, D. Akinwande, N. Alem, J. A. Schuller, R. E. Schaak, M. Terrones, J. A. Robinson, *ACS Nano* **2015**, *9*, 11509.
[9] W. Shi, J. Ye, Y. Zhang, R. Suzuki, M. Yoshida, J. Miyazaki, N. Inoue, Y. Saito, Y. Iwasa, *Sci. Rep.* **2015**, *5*, 12534.
[10] M. Sebek, Z. Wang, N. G. West, M. Yang, D. C. J. Neo, X. Su, S. Wang, J. Pan, N. T. K. Thanh, J. Teng, *npj 2D Mater. Appl.* **2024**, *8*, 9.
[11] R. Luo, W. W. Xu, Y. Zhang, Z. Wang, X. Wang, Y. Gao, P. Liu, M. Chen, *Nat. Commun.* **2020**, *11*, 1011.
[12] A. Chaves, J. G. Azadani, H. Alsalman, D. R. da Costa, R. Frisenda, A. J. Chaves, S. H. Song, Y. D. Kim, D. He, J. Zhou, A. Castellanos-Gomez, F. M. Peeters, Z. Liu, C. L. Hinkle, S.-H. Oh, P. D. Ye, S. J. Koester, Y. H. Lee, P. Avouris, X. Wang, T. Low, *npj 2D Mater. Appl.* **2020**, *4*, 29.
[13] J.-S. Kim, R. Ahmad, T. Pandey, A. Rai, S. Feng, J. Yang, Z. Lin, M. Terrones, S. K. Banerjee, A. K. Singh, D. Akinwande, J.-F. Lin, *2D Mater.* **2018**, *5*, 015008.
[14] J. Gusakova, X. Wang, L. L. Shiau, A. Krivosheeva, V. Shaposhnikov, V. Borisenko, V. Gusakov, B. K. Tay, *Phys. Status Solidi A* **2017**, *214*, 1700218.
[15] E. Blundo, M. Felici, T. Yildirim, G. Pettinari, D. Tedeschi, A. Miriametro, B. Liu, W. Ma, Y. Lu, A. Polimeni, *Phys. Rev. Res.* **2020**, *2*, 012024.
[16] B. Han, C. Robert, E. Courtade, M. Manca, S. Shree, T. Amand, P. Renucci, T. Taniguchi, K. Watanabe, X. Marie, L. E. Golub, M. M. Glazov, B. Urbaszek, *Phys. Rev. X* **2018**, *8*, 031073.
[17] T. Mueller, E. Malic, *npj 2D Mater. Appl.* **2018**, *2*, 29.
[18] Z. Nie, Y. Shi, S. Qin, Y. Wang, H. Jiang, Q. Zheng, Y. Cui, Y. Meng, F. Song, X. Wang, I. C. E. Turcu, X. Wang, Y. Xu, Y. Shi, J. Zhao, R. Zhang, F. Wang, *Commun. Phys.* **2019**, *2*, 103.
[19] J. Pu, T. Takenobu, *Adv. Mater.* **2018**, *30*, 1707627.
[20] R. Rosati, R. Perea-Causín, S. Brem, E. Malic, *Nanoscale* **2020**, *12*, 356.
[21] T. Handa, M. Holbrook, N. Olsen, L. N. Holtzman, L. Huber, H. I. Wang, M. Bonn, K. Barmak, J. C. Hone, A. N. Pasupathy, X. Zhu, *Sci. Adv.* **2024**, *10*, eadj4060.
[22] K. Xiao, R. Duan, Z. Liu, K. Watanabe, T. Taniguchi, W. Yao, X. Cui, *Nat. Sci.* **2023**, *3*, e20220035.
[23] F. Ceballos, Q. Cui, M. Z. Bellus, H. Zhao, *Nanoscale* **2016**, *8*, 11681.
[24] M. Aras, Ç. Kılıç, S. Ciraci, *J. Phys. Chem. C* **2018**, *122*, 1547.
[25] Z. Golsanamlou, P. Kumari, L. Sementa, T. Cusati, G. Iannaccone, A. Fortunelli, *Adv. Electron. Mater.* **2022**, *8*, 2200020.
[26] M.-Y. Li, C.-H. Chen, Y. Shi, L.-J. Li, *Mater. Today* **2016**, *19*, 322.
[27] R. Yang, J. Fan, M. Sun, *Front. Phys.* **2022**, *17*, 43202.

[28] S. H. Sung, Y. M. Goh, H. Yoo, R. Engelke, H. Xie, K. Zhang, Z. Li, A. Ye, P. B. Deotare, E. B. Tadmor, A. J. Mannix, J. Park, L. Zhao, P. Kim, R. Hovden, *Nat. Commun.* **2022**, *13*, 7826.
[29] S. Zhu, P. Pochet, H. T. Johnson, *ACS Nano* **2019**, *13*, 6925.
[30] J. Quan, L. Linhart, M.-L. Lin, D. Lee, J. Zhu, C.-Y. Wang, W.-T. Hsu, J. Choi, J. Embley, C. Young, T. Taniguchi, K. Watanabe, C.-K. Shih, K. Lai, A. H. MacDonald, P.-H. Tan, F. Libisch, X. Li, *Nat. Mater.* **2021**, *20*, 1100.
[31] J.-H. Baek, H. G. Kim, S. Y. Lim, S. C. Hong, Y. Chang, H. Ryu, Y. Jung, H. Jang, J. Kim, Y. Zhang, K. Watanabe, T. Taniguchi, P. Y. Huang, H. Cheong, M. Kim, G.-H. Lee, *Nat. Mater.* **2023**, *22*, 1463.
[32] Á. Rodríguez, J. Varillas, G. Haider, M. Kalbáč, O. Frank, *ACS Nano* **2023**, *17*, 7787.
[33] A. Weston, Y. Zou, V. Enaldiev, A. Summerfield, N. Clark, V. Zólyomi, A. Graham, C. Yelgel, S. Magorrian, M. Zhou, J. Zultak, D. Hopkinson, A. Barinov, T. H. Bointon, A. Kretinin, N. R. Wilson, P. H. Beton, V. I. Fal'ko, S. J. Haigh, R. Gorbachev, *Nat. Nanotechnol.* **2020**, *15*, 592.
[34] M. R. Rosenberger, H.-J. Chuang, M. Phillips, V. P. Oleshko, K. M. McCreary, S. V. Sivaram, C. S. Hellberg, B. T. Jonker, *ACS Nano* **2020**, *14*, 4550.
[35] W.-M. Zhao, L. Zhu, Z. Nie, Q.-Y. Li, Q.-W. Wang, L.-G. Dou, J.-G. Hu, L. Xian, S. Meng, S.-C. Li, *Nat. Mater.* **2022**, *21*, 284.
[36] W. Li, T. Brumme, T. Heine, *npj 2D Mater. Appl.* **2024**, *8*, 43.
[37] S. Zhu, H. T. Johnson, *Nanoscale* **2018**, *10*, 20689.
[38] F. M. Arnold, A. Ghasemifard, A. Kuc, J. Kunstmann, T. Heine, *2D Mater.* **2023**, *10*, 045010.
[39] W. Qiu, B. Zhang, Y. Sun, L. He, Y. Ni, *Extreme Mech. Lett.* **2024**, *69*, 102159.
[40] E. Li, J.-X. Hu, X. Feng, Z. Zhou, L. An, K. T. Law, N. Wang, N. Lin, *Nat. Commun.* **2021**, *12*, 5601.
[41] L. Wang, E.-M. Shih, A. Ghiotto, L. Xian, D. A. Rhodes, C. Tan, M. Claassen, D. M. Kennes, Y. Bai, B. Kim, K. Watanabe, T. Taniguchi, X. Zhu, J. Hone, A. Rubio, A. N. Pasupathy, C. R. Dean, *Nat. Mater.* **2020**, *19*, 861.
[42] Z. Bi, L. Fu, *Nat. Commun.* **2021**, *12*, 642.
[43] A. C. Dias, F. Qu, D. L. Azevedo, J. Fu, *Phys. Rev. B* **2018**, *98*, 075202.
[44] S. K. Pandey, R. Das, P. Mahadevan, *ACS Omega* **2020**, *5*, 15169.
[45] T. Wang, X. Tan, Y. Wei, H. Jin, *Nanoscale* **2022**, *14*, 2511.
[46] M. Berg, K. Keyshar, I. Bilgin, F. Liu, H. Yamaguchi, R. Vajtai, C. Chan, G. Gupta, S. Kar, P. Ajayan, T. Ohta, A. D. Mohite, *Phys. Rev. B* **2017**, *95*, 235406.
[47] H. Li, A. Ji, C. Zhu, L. Cui, L.-F. Mao, *J. Phys. Chem. Solids* **2020**, *139*, 109331.
[48] K. F. Mak, C. Lee, J. Hone, J. Shan, T. F. Heinz, *Phys. Rev. Lett.* **2010**, *105*, 136805.
[49] J. Xia, J. Yan, Z. X. Shen, *FlatChem* **2017**, *4*, 1.
[50] W. Zhang, D. Chang, Q. Gao, C. Niu, C. Li, F. Wang, X. Huang, C. Xia, Y. Jia, *J. Phys. Chem. C* **2018**, *6*, 10256.
[51] W. Hu, T. Wang, R. Zhang, J. Yang, *J. Phys. Chem. C* **2016**, *4*, 1776.
[52] H. V. Phuc, N. N. Hieu, B. D. Hoi, C. V. Nguyen, *Phys. Chem. Chem. Phys.* **2018**, *20*, 17899.
[53] A. Kormányos, V. Zólyomi, V. I. Fal'ko, G. Burkard, *Phys. Rev. B* **2018**, *98*, 035408.
[54] X. Li, X. Shi, D. Marian, D. Soriano, T. Cusati, G. Iannaccone, G. Fiori, Q. Guo, W. Zhao, Y. Wu, *Sci. Adv.* **2023**, *9*, eade5706.
[55] F. Wu, T. Lovorn, E. Tutuc, I. Martin, A. H. MacDonald, *Phys. Rev. Lett.* **2019**, *122*, 086402.
[56] T. Devakul, V. Crépel, Y. Zhang, L. Fu, *Nat. Commun.* **2021**, *12*, 6730.
[57] Z. Zhang, Y. Wang, K. Watanabe, T. Taniguchi, K. Ueno, E. Tutuc, B. J. LeRoy, *Nat. Phys.* **2020**, *16*, 1093.
[58] V. Vitale, K. Atalar, A. A. Mostofi, J. Lischner, *2D Mater.* **2021**, *8*, 045010.
[59] H. Pan, F. Wu, S. D Sarma, *Phys. Rev. Res.* **2020**, *2*, 033087.
[60] J. Zang, J. Wang, J. Cano, A. J. Millis, *Phys. Rev. B* **2021**, *104*, 075150.
[61] H. C. Po, L. Zou, A. Vishwanath, T. Senthil, *Phys. Rev. X* **2018**, *8*, 031089.
[62] Y. Cao, V. Fatemi, S. Fang, K. Watanabe, T. Taniguchi, E. Kaxiras, P. Jarillo-Herrero, *Nature* **2018**, *556*, 43.
[63] Y. Xia, Z. Han, K. Watanabe, T. Taniguchi, J. Shan, K. F. Mak, *Nature* **2025**, *637*, 833.
[64] M. M. Scherer, D. M. Kennes, L. Classen, *npj Quantum Mater.* **2022**, *7*, 100.
[65] C. Ma, S. Yuan, P. Cheung, K. Watanabe, T. Taniguchi, F. Zhang, F. Xia, *Nature* **2022**, *604*, 266.
[66] C. Nayak, S. H. Simon, A. Stern, M. Freedman, S. D Sarma, *Rev. Mod. Phys.* **2008**, *80*, 1083.
[67] Y. Jiang, S. Chen, W. Zheng, B. Zheng, A. Pan, *Light Sci. Appl.* **2021**, *10*, 72.
[68] H. Fang, C. Battaglia, C. Carraro, S. Nemsak, B. Ozdol, J. S. Kang, H. A. Bechtel, S. B. Desai, F. Kronast, A. A. Unal, G. Conti, C. Conlon, G. K. Palsson, M. C. Martin, A. M. Minor, C. S. Fadley, E. Yablonovitch, R. Maboudian, A. Javey, *Proc. Natl. Acad. Sci. USA* **2014**, *111*, 6198.
[69] M.-H. Chiu, M.-Y. Li, W. Zhang, W.-T. Hsu, W.-H. Chang, M. Terrones, H. Terrones, L.-J. Li, *ACS Nano.* **2014**, *8*, 9649.
[70] P. Rivera, J. R. Schaibley, A. M. Jones, J. S. Ross, S. Wu, G. Aivazian, P. Klement, K. Seyler, G. Clark, N. J. Ghimire, J. Yan, D. G. Mandrus, W. Yao, X. Xu, *Nat. Commun.* **2015**, *6*, 6242.
[71] P. Nagler, G. Plechinger, M. V. Ballottin, A. Mitioglu, S. Meier, N. Paradiso, C. Strunk, A. Chernikov, P. C. M. Christianen, C. Schüller, T. Korn, *2D Mater.* **2017**, *4*, 025112.
[72] L. A. Jauregui, A. Y. Joe, K. Pistunova, D. S. Wild, A. A. High, Y. Zhou, G. Scuri, K. De Greve, A. Sushko, C.-H. Yu, T. Taniguchi, K. Watanabe, D. J. Needleman, M. D. Lukin, H. Park, P. Kim, *Science* **2019**, *366*, 870.
[73] W. Liu, presented at *2013 IEEE Int. Electron Devices Meet.* , Washington D.C., December **2013**.
[74] K. M. McCreary, M. Phillips, H.-J. Chuang, D. Wickramaratne, M. Rosenberger, C. S. Hellberg, B. T. Jonker, *Nanoscale* **2022**, *14*, 147.
[75] T. Cusati, A. Fortunelli, G. Fiori, G. Iannaccone, *Phys. Rev. B* **2018**, *98*, 115403.
[76] N. Jiang, J. Shi, H. Wu, D. Zhang, H. Zhu, X. Liu, P.-H. Tan, K. Chang, H. Zheng, C. Shen, *Adv. Opt. Mater.* **2023**, *11*, 2300458.
[77] I. Paradisanos, S. Shree, A. George, N. Leisgang, C. Robert, K. Watanabe, T. Taniguchi, R. J. Warburton, A. Turchanin, X. Marie, I. C. Gerber, B. Urbaszek, *Nat. Commun.* **2020**, *11*, 2391.
[78] Z. Zeng, X. Sun, D. Zhang, W. Zheng, X. Fan, M. He, T. Xu, L. Sun, X. Wang, A. Pan, *Adv. Funct. Mater.* **2019**, *29*, 1806874.
[79] K. Liu, L. Zhang, T. Cao, C. Jin, D. Qiu, Q. Zhou, A. Zettl, P. Yang, S. G. Louie, F. Wang, *Nat. Commun.* **2014**, *5*, 4966.
[80] Z. Li, J. Förste, K. Watanabe, T. Taniguchi, B. Urbaszek, A. S. Baimuratov, I. C. Gerber, A. Högele, I. Bilgin, *Phys. Rev. B* **2022**, *106*, 045411.
[81] C. Jin, E. C. Regan, A. Yan, M. Iqbal Bakti Utama, D. Wang, S. Zhao, Y. Qin, S. Yang, Z. Zheng, S. Shi, K. Watanabe, T. Taniguchi, S. Tongay, A. Zettl, F. Wang, *Nature* **2019**, *567*, 76.
[82] L. Zhang, Z. Zhang, F. Wu, D. Wang, R. Gogna, S. Hou, K. Watanabe, T. Taniguchi, K. Kulkarni, T. Kuo, S. R. Forrest, H. Deng, *Nat. Commun.* **2020**, *11*, 5888.
[83] H. Guo, X. Zhang, G. Lu, *Sci. Adv.* **2020**, *6*, eabc5638.
[84] L. Yuan, B. Zheng, J. Kunstmann, T. Brumme, A. B. Kuc, C. Ma, S. Deng, D. Blach, A. Pan, L. Huang, *Nat. Mater.* **2020**, *19*, 617.
[85] J. Choi, M. Florian, A. Steinhoff, D. Erben, K. Tran, D. S. Kim, L. Sun, J. Quan, R. Claassen, S. Majumder, J. A. Hollingsworth, T. Taniguchi, K. Watanabe, K. Ueno, A. Singh, G. Moody, F. Jahnke, X. Li, *Phys. Rev. Lett.* **2021**, *126*, 047401.
[86] D. Huang, J. Choi, C.-K. Shih, X. Li, *Nat. Nanotechnol.* **2022**, *17*, 227.
[87] S. Brem, C. Linderälv, P. Erhart, E. Malic, *Nano Lett.* **2020**, *20*, 8534.

[88] S. Shabani, D. Halbertal, W. Wu, M. Chen, S. Liu, J. Hone, W. Yao, D. N. Basov, X. Zhu, A. N. Pasupathy, *Nat. Phys.* **2021**, *17*, 720.
[89] S. Kundu, T. Amit, H. R. Krishnamurthy, M. Jain, S. Refaely-Abramson, *npj Comput. Mater.* **2023**, *9*, 186.
[90] J. Hagel, S. Brem, J. A. Pineiro, E. Malic, *Phys. Rev. Mater.* **2024**, *8*, 034001.
[91] K. L. Seyler, P. Rivera, H. Yu, N. P. Wilson, E. L. Ray, D. G. Mandrus, J. Yan, W. Yao, X. Xu, *Nature* **2019**, *567*, 66.
[92] A. Rossi, J. Zipfel, I. Maity, M. Lorenzon, M. Dandu, E. Barré, L. Francaviglia, E. C. Regan, Z. Zhang, J. H. Nie, E. S. Barnard, K. Watanabe, T. Taniguchi, E. Rotenberg, F. Wang, J. Lischner, A. Raja, A. Weber-Bargioni, *ACS Nano* **2024**, *18*, 18202.
[93] H. Zheng, B. Wu, C.-T. Wang, S. Li, J. He, Z. Liu, J.-T. Wang, J.-a. Duan, Y. Liu, *Small* **2023**, *19*, 2207988.
[94] C. C. Palekar, P. E. Faria Junior, B. Rosa, F. B. Sousa, L. M. Malard, J. Fabian, S. Reitzenstein, *npj 2D Mater. Appl.* **2024**, *8*, 49.
[95] B. Wu, H. Zheng, S. Li, C.-T. Wang, J. Ding, J. He, Z. Liu, J.-T. Wang, Y. Liu, *ACS Appl. Mater. Interfaces* **2023**, *15*, 48475.
[96] F. Volmer, M. Ersfeld, P. E. Faria Junior, L. Waldecker, B. Parashar, L. Rathmann, S. Dubey, I. Cojocariu, V. Feyer, K. Watanabe, T. Taniguchi, C. M. Schneider, L. Plucinski, C. Stampfer, J. Fabian, B. Beschoten, *npj 2D Mater. Appl.* **2023**, *7*, 58.
[97] R. Wang, K. Chang, W. Duan, Y. Xu, P. Tang, *Phys. Rev. Lett.* **2025**, *134*, 026904.
[98] A. R. Montblanch, M. Barbone, I. Aharonovich, M. Atature, A. C. Ferrari, *Nat. Nanotechnol.* **2023**, *18*, 555.
[99] G. Scuri, T. I. Andersen, Y. Zhou, D. S. Wild, J. Sung, R. J. Gelly, D. Berube, H. Heo, L. Shao, A. Y. Joe, A. M. Mier Valdivia, T. Taniguchi, K. Watanabe, M. Loncar, P. Kim, M. D. Lukin, H. Park, *Phys. Rev. Lett.* **2020**, *124*, 217403.
[100] Y. Liu, Y. Gao, S. Zhang, J. He, J. Yu, Z. Liu, *Nano Res.* **2019**, *12*, 2695.
[101] D. Dai, B. Fu, J. Yang, L. Yang, S. Yan, X. Chen, H. Li, Z. Zuo, C. Wang, K. Jin, Q. Gong, X. Xu, *Sci. Adv.* **2024**, *10*, eado1281.
[102] K. Zhou, D. Wickramaratne, S. Ge, S. Su, A. De, R. K. Lake, *Phys. Chem. Chem. Phys.* **2017**, *19*, 10406.
[103] M. Liao, Z. Wei, L. Du, Q. Wang, J. Tang, H. Yu, F. Wu, J. Zhao, X. Xu, B. Han, K. Liu, P. Gao, T. Polcar, Z. Sun, D. Shi, R. Yang, G. Zhang, *Nat. Commun.* **2020**, *11*, 2153.
[104] Z. Liu, F. Liu, Y.-S. Wu, *Chin. Phys. B* **2014**, *23*, 077308.
[105] Y. Guo, J. Pack, J. Swann, L. Holtzman, M. Cothrine, K. Watanabe, T. Taniguchi, D. G. Mandrus, K. Barmak, J. Hone, A. J. Millis, A. Pasupathy, C. R. Dean, *Nature* **2025**, *637*, 839.
[106] L. Cardarelli, S. Julià-Farré, M. Lewenstein, A. Dauphin, M. Müller, *Quantum Sci. Technol.* **2023**, *8*, 025018.
[107] K. F. Mak, J. Shan, *Nat. Nanotechnol.* **2022**, *17*, 686.
[108] J. Cai, E. Anderson, C. Wang, X. Zhang, X. Liu, W. Holtzmann, Y. Zhang, F. Fan, T. Taniguchi, K. Watanabe, Y. Ran, T. Cao, L. Fu, D. Xiao, W. Yao, X. Xu, *Nature* **2023**, *622*, 63.
[109] H. Park, J. Cai, E. Anderson, Y. Zhang, J. Zhu, X. Liu, C. Wang, W. Holtzmann, C. Hu, Z. Liu, T. Taniguchi, K. Watanabe, J.-H. Chu, T. Cao, L. Fu, W. Yao, C.-Z. Chang, D. Cobden, D. Xiao, X. Xu, *Nature* **2023**, *622*, 74.
[110] T. Li, S. Jiang, B. Shen, Y. Zhang, L. Li, Z. Tao, T. Devakul, K. Watanabe, T. Taniguchi, L. Fu, J. Shan, K. F. Mak, *Nature* **2021**, *600*, 641.
[111] D. Xiao, M.-C. Chang, Q. Niu, *Rev. Mod. Phys.* **2010**, *82*, 1959.
[112] N. Nagaosa, J. Sinova, S. Onoda, A. H. MacDonald, N. P. Ong, *Rev. Mod. Phys.* **2010**, *82*, 1539.
[113] B. T. Zhou, K. Taguchi, Y. Kawaguchi, Y. Tanaka, K. T. Law, *Commun. Phys.* **2019**, *2*, 26.
[114] C. Ortix, *Adv. Quantum Technol.* **2021**, *4*, 2100056.
[115] T. Chakraborty, K. Samanta, S. N. Guin, J. Noky, I. Robredo, S. Prasad, J. Kuebler, C. Shekhar, M. G. Vergniory, C. Felser, *Phys. Rev. B* **2022**, *106*, 155141.
[116] S. Bera, S. Chatterjee, S. Pradhan, S. K. Pradhan, S. Kalimuddin, A. Bera, A. K. Nandy, M. Mondal, *Phys. Rev. B* **2023**, *108*, 115122.
[117] S. Korrapati, S. Nandy, S. Tewari, *Phys. Rev. B* **2024**, *110*, 195119.
[118] A. Tiwari, F. Chen, S. Zhong, E. Drueke, J. Koo, A. Kaczmarek, C. Xiao, J. Gao, X. Luo, Q. Niu, Y. Sun, B. Yan, L. Zhao, A. W. Tsen, *Nat. Commun.* **2021**, *12*, 2049.
[119] V. Crépel, N. Regnault, R. Queiroz, *Commun. Phys.* **2024**, *7*, 146.
[120] A. P. Reddy, F. Alsallom, Y. Zhang, T. Devakul, L. Fu, *Phys. Rev. B* **2023**, *108*, 085117.
[121] S. D Sarma, M. Xie, *Phys. Rev. B* **2024**, *109*, L121104.
[122] V. Crépel, L. Fu, *Phys. Rev. B* **2023**, *107*, L201109.
[123] M. Wu, J. Li, *Proc. Natl. Acad. Sci.* **2021**, *118*, e2115703118.
[124] A. Weston, E. G. Castanon, V. Enaldiev, F. Ferreira, S. Bhattacharjee, S. Xu, H. Corte-León, Z. Wu, N. Clark, A. Summerfield, T. Hashimoto, Y. Gao, W. Wang, M. Hamer, H. Read, L. Fumagalli, A. V. Kretinin, S. J. Haigh, O. Kazakova, A. K. Geim, V. I. Fal'ko, R. Gorbachev, *Nat. Nanotechnol.* **2022**, *17*, 390.
[125] X. Wang, K. Yasuda, Y. Zhang, S. Liu, K. Watanabe, T. Taniguchi, J. Hone, L. Fu, P. Jarillo-Herrero, *Nat. Nanotechnol.* **2022**, *17*, 367.
[126] S. Deb, W. Cao, N. Raab, K. Watanabe, T. Taniguchi, M. Goldstein, L. Kronik, M. Urbakh, O. Hod, M. Ben Shalom, *Nature* **2022**, *612*, 465.
[127] T. H. Yang, B.-W. Liang, H.-C. Hu, F.-X. Chen, S.-Z. Ho, W.-H. Chang, L. Yang, H.-C. Lo, T.-H. Kuo, J.-H. Chen, P.-Y. Lin, K. B. Simbulan, Z.-F. Luo, A. C. Chang, Y.-H. Kuo, Y.-S. Ku, Y.-C. Chen, Y.-J. Huang, Y.-C. Chang, Y.-F. Chiang, T.-H. Lu, M.-H. Lee, K.-S. Li, M. Wu, Y.-C. Chen, C.-L. Lin, Y.-W. Lan, *Nat. Electron.* **2024**, *7*, 29.
[128] K. Ko, A. Yuk, R. Engelke, S. Carr, J. Kim, D. Park, H. Heo, H.-M. Kim, S.-G. Kim, H. Kim, T. Taniguchi, K. Watanabe, H. Park, E. Kaxiras, S. M. Yang, P. Kim, H. Yoo, *Nat. Mater.* **2023**, *22*, 992.
[129] P. Tang, G. E. W. Bauer, *Phys. Rev. Lett.* **2023**, *130*, 176801.
[130] K. Yasuda, E. Zalys-Geller, X. Wang, D. Bennett, S. S. Cheema, K. Watanabe, T. Taniguchi, E. Kaxiras, P. Jarillo-Herrero, R. Ashoori, *Science* **2024**, *385*, 53.
[131] Z. Fei, W. Zhao, T. A. Palomaki, B. Sun, M. K. Miller, Z. Zhao, J. Yan, X. Xu, D. H. Cobden, *Nature* **2018**, *560*, 336.
[132] S. Zhang, Y. Liu, Z. Sun, X. Chen, B. Li, S. L. Moore, S. Liu, Z. Wang, S. E. Rossi, R. Jing, J. Fonseca, B. Yang, Y. Shao, C.-Y. Huang, T. Handa, L. Xiong, M. Fu, T.-C. Pan, D. Halbertal, X. Xu, W. Zheng, P. J. Schuck, A. N. Pasupathy, C. R. Dean, X. Zhu, D. H. Cobden, X. Xu, M. Liu, M. M. Fogler, J. C. Hone, et al., *Nat. Commun.* **2023**, *14*, 6200.
[133] R. Bian, R. He, E. Pan, Z. Li, G. Cao, P. Meng, J. Chen, Q. Liu, Z. Zhong, W. Li, F. Liu, *Science* **2024**, *385*, 57.
[134] A. C. Gadelha, D. A. A. Ohlberg, C. Rabelo, E. G. S. Neto, T. L. Vasconcelos, J. L. Campos, J. S. Lemos, V. Ornelas, D. Miranda, R. Nadas, F. C. Santana, K. Watanabe, T. Taniguchi, B. van Troeye, M. Lamparski, V. Meunier, V.-H. Nguyen, D. Paszko, J.-C. Charlier, L. C. Campos, L. G. Cançado, G. Medeiros-Ribeiro, A. Jorio, *Nature* **2021**, *590*, 405.
[135] K. Kim, M. Yankowitz, B. Fallahazad, S. Kang, H. C. P. Movva, S. Huang, S. Larentis, C. M. Corbet, T. Taniguchi, K. Watanabe, S. K. Banerjee, B. J. LeRoy, E. Tutuc, *Nano Lett.* **2016**, *16*, 1989.
[136] K. Kim, A. DaSilva, S. Huang, B. Fallahazad, S. Larentis, T. Taniguchi, K. Watanabe, B. J. LeRoy, A. H. MacDonald, E. Tutuc, *Proc. Natl. Acad. Sci.* **2017**, *114*, 3364.
[137] X. Zhang, H. Nan, S. Xiao, X. Wan, X. Gu, A. Du, Z. Ni, K. Ostrikov, *Nat. Commun.* **2019**, *10*, 598.
[138] C. Chang, X. Zhang, W. Li, Q. Guo, Z. Feng, C. Huang, Y. Ren, Y. Cai, X. Zhou, J. Wang, Z. Tang, F. Ding, W. Wei, K. Liu, X. Xu, *Nat. Commun.* **2024**, *15*, 4130.
[139] M. Xu, H. Ji, L. Zheng, W. Li, J. Wang, H. Wang, L. Luo, Q. Lu, X. Gan, Z. Liu, X. Wang, W. Huang, *Nat. Commun.* **2024**, *15*, 562.

[140] L. Liu, T. Li, L. Ma, W. Li, S. Gao, W. Sun, R. Dong, X. Zou, D. Fan, L. Shao, C. Gu, N. Dai, Z. Yu, X. Chen, X. Tu, Y. Nie, P. Wang, J. Wang, Y. Shi, X. Wang, *Nature* **2022**, *605*, 69.
[141] R. Dong, X. Gong, J. Yang, Y. Sun, L. Ma, J. Wang, *Adv. Mater.* **2022**, *34*, 2201402.
[142] B. Qin, C. Ma, Q. Guo, X. Li, W. Wei, C. Ma, Q. Wang, F. Liu, M. Zhao, G. Xue, J. Qi, M. Wu, H. Hong, L. Du, Q. Zhao, P. Gao, X. Wang, E. Wang, G. Zhang, C. Liu, K. Liu, *Science* **2024**, *385*, 99.
[143] D. Moon, W. Lee, C. Lim, J. Kim, J. Kim, Y. Jung, H.-Y. Choi, W. S. Choi, H. Kim, J.-H. Baek, C. Kim, J. Joo, H.-G. Oh, H. Jang, K. Watanabe, T. Taniguchi, S. Bae, J. Son, H. Ryu, J. Kwon, H. Cheong, J. W. Han, H. Jang, G.-H. Lee, *Nature* **2025**, *638*, 957.
[144] D. Sarkar, X. Xie, W. Liu, W. Cao, J. Kang, Y. Gong, S. Kraemer, P. M. Ajayan, K. Banerjee, *Nature* **2015**, *526*, 91.
[145] Z. Wang, Q. Li, Y. Chen, B. Cui, Y. Li, F. Besenbacher, M. Dong, *NPG Asia Mater* **2018**, *10*, 703.
[146] G. Lee, S. Oh, J. Kim, J. Kim, *ACS Appl. Mater. Interfaces* **2020**, *12*, 23127.
[147] J. Kwon, J.-Y. Lee, Y.-J. Yu, C.-H. Lee, X. Cui, J. Hone, G.-H. Lee, *Nanoscale* **2017**, *9*, 6151.
[148] S. Park, J. Ha, M. F. Khan, C. Im, J. Y. Park, S. H. Yoo, M. A. Rehman, K. Kang, S. H. Lee, S. C. Jun, *ACS Appl. Electron. Mater.* **2022**, *4*, 4306.
[149] D. Unuchek, A. Ciarrocchi, A. Avsar, K. Watanabe, T. Taniguchi, A. Kis, *Nature* **2018**, *560*, 340.
[150] F. Tagarelli, E. Lopriore, D. Erkensten, R. Perea-Causín, S. Brem, J. Hagel, Z. Sun, G. Pasquale, K. Watanabe, T. Taniguchi, E. Malic, A. Kis, *Nat. Photonics* **2023**, *17*, 615.
[151] H. Baek, M. Brotons-Gisbert, Z. X. Koong, A. Campbell, M. Rambach, K. Watanabe, T. Taniguchi, B. D. Gerardot, *Sci. Adv.* **2020**, *6*, eaba8526.
[152] A. B. D. Shaik, P. Palla, *Sci. Rep.* **2021**, *11*, 12285.
[153] H. Yang, Y. Hu, X. Zhang, Y. Ding, S. Wang, Z. Su, Y. Shuai, P. Hu, *Adv. Funct. Mater.* **2024**, *34*, 2308149.
[154] Y. Hassan, B. Singh, M. Joe, B.-M. Son, T. D. Ngo, Y. Jang, S. Sett, A. Singha, R. Biswas, M. Bhakar, K. Watanabe, T. Taniguchi, V. Raghunathan, G. Sheet, Z. Lee, W. J. Yoo, P. K. Srivastava, C. Lee, *Adv. Mater.* **2024**, *36*, 2406290.
[155] M. Si, A. K. Saha, S. Gao, G. Qiu, J. Qin, Y. Duan, J. Jian, C. Niu, H. Wang, W. Wu, S. K. Gupta, P. D. Ye, *Nat. Electron.* **2019**, *2*, 580.
[156] C. Wang, Y. Zhang, D. Zhang, Y. Sun, T. Zhang, J. Li, *Small* **2025**, e2408375.
[157] X. Sun, Q. Xia, T. Cao, S. Yuan, *Mater. Sci. Eng. R Rep.* **2025**, *163*, 100927.
[158] L. Rogée, L. Wang, Y. Zhang, S. Cai, P. Wang, M. Chhowalla, W. Ji, S. P. Lau, *Science* **2022**, *376*, 973.
[159] G. Yuan, W. Liu, X. Huang, Z. Wan, C. Wang, B. Yao, W. Sun, H. Zheng, K. Yang, Z. Zhou, Y. Nie, J. Xu, L. Gao, *Nat. Commun.* **2023**, *14*, 5457.
[160] M. Nakatani, S. Fukamachi, P. Solís-Fernández, S. Honda, K. Kawahara, Y. Tsuji, Y. Sumiya, M. Kuroki, K. Li, Q. Liu, Y.-C. Lin, A. Uchida, S. Oyama, H. G. Ji, K. Okada, K. Suenaga, Y. Kawano, K. Yoshizawa, A. Yasui, H. Ago, *Nat. Electron.* **2024**, *7*, 119.
[161] S. Fukamachi, P. Solís-Fernández, K. Kawahara, D. Tanaka, T. Otake, Y.-C. Lin, K. Suenaga, H. Ago, *Nat. Electron.* **2023**, *6*, 126.
[162] Y. Zhao, Y. Song, Z. Hu, W. Wang, Z. Chang, Y. Zhang, Q. Lu, H. Wu, J. Liao, W. Zou, X. Gao, K. Jia, L. Zhuo, J. Hu, Q. Xie, R. Zhang, X. Wang, L. Sun, F. Li, L. Zheng, M. Wang, J. Yang, B. Mao, T. Fang, F. Wang, H. Zhong, W. Liu, R. Yan, J. Yin, Y. Zhang, et al., *Nat. Commun.* **2022**, *13*, 4409.

Hyun-Geun Oh received his B.S. (2018) in the Department of Materials Science and Engineering from Yonsei University. Then, he has studied at Seoul National University in Ph.D. course. His research is focused on wafer-scale high-quality transition metal dichalcogenides growth via metal–organic chemical vapor deposition.

Younghyun You is Senior Engineer at Samsung Electronics. He received his M.S. (2017) in the Department of Materials Science and Engineering at Korea Advanced Institute of Science and Technology. Then, he has studied at Seoul National University in Ph.D. course. His research is focused on the realization of next-generation devices using transition metal dichalcogenides.

Seungyun Lee received his B.S. (2023) in the Department of Chemical and Biomolecular Engineering from Yonsei University. Then, he has studied at Seoul National University in Ph.D. course. His research is focused on contact engineering of transition metal dichalcogenides.

Sangheon Lee is an Associate Professor at Ewha Womans University. In 2010, he received Ph.D. in Chemical Engineering from The University of Texas at Austin. Then, he joined the Max Planck Institute for Sustainable Materials as a postdoctoral researcher. In 2013, he joined the Korea Institute of Science and Technology as a postdoctoral researcher. His research activities include scale-bridging computer simulations for semiconductor surface processing and energy materials.

Fan Ren is a Distinguished Professor of Chemical Engineering at the University of Florida, Gainesville, FL, USA. He joined UF in 1997 after 12 years as a member of Technical Staff at AT&T Bell Laboratories, where he was responsible for high-speed compound semiconductor device development. He is a Fellow of SPIE, ECS, IEEE, APS, MRS, and AVS. His interests lie in novel semiconductor devices.

Stephen J. Pearton is a Distinguished Professor of Materials Science and Engineering at the University of Florida, Gainesville, FL, USA. He has a Ph.D. in Physics from the University of Tasmania and was a postdoctoral researcher at UC Berkeley prior to working at AT&T Bell Laboratories from 1984–1994. His interests are in the electronic and optical properties of semiconductors. He is a Fellow of the IEEE, AVS, ECS, TMS, MRS, SPIE, and APS.

Jihyun Kim is a Professor at the Department of Chemical and Biological Engineering at Seoul National University. He received his BS from Seoul National University, and Ph.D. from the University of Florida. Then, he joined the US Naval Research Laboratory to work on the optical/electrical analysis of wide-bandgap semiconductors. He is a Fellow of the Electrochemical Society (ECS).

Gwan-Hyoung Lee is a Professor at Seoul National University. He received Ph.D. in Materials Science and Engineering from SNU. Then, he worked for Samsung Electronics. In 2010, he joined Columbia University as a postdoctoral researcher. After five years at Yonsei University, he is now with SNU since 2019. His research activities include the investigations of electrical, mechanical, and optical properties of 2D materials as well as 2D-material-based heterostructure devices for electrical and optoelectronic applications.